EXPLOITING SUBSURFACE OCEAN DYNAMICS FOR DECADAL PREDICTABILITY IN THE UPWELLING SYSTEMS OF THE EASTERN NORTH PACIFIC

A Dissertation
Presented to
The Academic Faculty

by

María Mercedes Pozo Buil

In Partial Fulfillment
of the Requirements for the Degree
Doctor of Philosophy in the
School of Earth and Atmospheric Sciences

Georgia Institute of Technology
December 2017

EXPLOITING SUBSURFACE OCEAN DYNAMICS FOR DECADAL PREDICTABILITY IN THE UPWELLING SYSTEMS OF THE EASTERN NORTH PACIFIC

Approved by:

Dr. Emanuele Di Lorenzo, Advisor
School of Earth and Atmospheric Sciences
Georgia Institute of Technology

Dr. Annalisa Bracco
School of Earth and Atmospheric Sciences
Georgia Institute of Technology

Dr. Taka Ito
School of Earth and Atmospheric Sciences
Georgia Institute of Technology

Dr. Kim Cobb
School of Earth and Atmospheric Sciences
Georgia Institute of Technology

Dr. Steven Bograd
National Oceanic and Atmospheric
Administration (NOAA)

Date Approved: November 3, 2017

A mi madre, la mujer de mi vida, por su amor y apoyo incondicional.

Y a mi padre, que desde el cielo sigue mirando por mí.

ACKNOWLEDGEMENTS

I would like to express my sincerest gratitude and appreciation to my advisor Dr. Emanuele Di Lorenzo. I could not have asked for better guidance and support than you have given me during this journey. Thank you for giving me this opportunity to learn from you. I owe you an ocean of gratitude for your patience, support, and enthusiasm. Thank you for believing in me and for seeing more strengths than weaknesses. You will always be more than my academic advisor.

I would like to extend my gratitude to all the members of my doctoral committee. To Dr. Annalisa Bracco and Dr. Taka Ito, thank you for your invaluable classes, feedback, and assistance when I needed it. I also would like to thank all the faculty and staff of the School of Earth and Atmospheric Sciences and of Georgia Institute of Technology, who were always willing to help.

Thanks also to Dr. Dana Hartley for being a fabulous teaching mentor. My first steps in my teaching experience would have been very different without your guidance and your contagious energy. Thank you for always receiving me with your enormous smile.

I wish to thank all my friends, the old and the new, for their part in my grad school journey. To my "everything is awesome" office mates and the multicultural international oceanography EAS group, especially to Seb, Yohei, Youngji, Fabri, Fil, and Anh, thanks for the everyday laughs. You are the best. Thanks, Sebastian, for all the laughs and "Spanish from Spain" fights. I could have never imagined that at the end I would speak a

little Colombian. I also want to thank my friend, Hussein, for his support and advice during this last year. I also appreciate those friends who are always there, no matter the distance. To Ricardo and Juanlu, we started this crazy adventure together and finally we finished. I wish we just lived a little closer to see you more often. And of course to the strongest person that I know, my best friend Valme, thanks for always being there for me everyday, no matter the time or the day. We still have a lot of things to live together.

My special gratitude and love goes out to my family, specially to my mum, my brothers, and my sister, for their unfailing support. I would not be here without all you. Thanks to the best partner in this journey, Mike, I think there are not enough words to thank you for your everyday patience, for being by my side, and for encouraging me to pursue my dreams. Lastly, I would love to express my deepest love and thanks to my mum for her unconditional love and for being the pillar of strength in my life. Also I would like to thank my dad, that even though he is not in this world anymore, I know he is up there, listening and watching me. You are still alive in my thoughts and my heart everyday.

Finally, and foremost, I would like to thank God for giving me the strength, knowledge, ability, and perseverance to enable me to accomplish this achievement.

TABLE OF CONTENTS

LIST OF TABLES

LIST OF FIGURES

LIST OF SYMBOLS AND ABBREVIATIONS

AR1	Autoregressive order one
CaLCOFI	California Cooperative Fisheries Investigations
CC	California Current
CCS	California Current System
CU	California Undercurrent
dQdSST	Net heat flux sensitivity to SST
ECMWF	European Centre for Medium-range Weather Forecasting
EOF	Empirical Orthogonal Function
GOA	Gulf of Alaska
KPP	K-profile parametrization
KOE	Kuroshio-Oyashio Extension
LF–AM3 PC	Leap-Frog third-order Adams-Moulton predictor-corrector
NCAR	National Center for Atmospheric Research
NCEP	National Center for Environmental Prediction
NOAA	National Oceanic and Atmospheric Admisnistration
NPC	North Pacific Current
NPGO	North Pacific Gyre Oscillation
OMZ	Oxygen minimum zones
ORA-S	Ocean Reanalysis System
OSP	Ocean Station PAPA
PC	Principal Component
PDF	Probability distribution function

PDO	Pacific Decadal Oscillation
PNA	Pacific North American
R	Correlation coefficient
ROMS	Regional Ocean Modeling System
ROMS12	12 km ROMS model
ROSM23	23 km ROMS model
σ_θ	Potential density
SCB	Southern California Bight
SLPa	Anomalous Sea Level Pressure
SSS	Sea Surface Salinity
SST	Sea Surface Temperature
SSTa	Sea Surface Temperature anomalies
SODA	Simple Ocean Data Assimilation
SWFLUX	Surface net freshwater flux
τ	Damping time scale
T'_{sub}	Subsurface temperature anomalies at the base of the Ekman layer
$\bar{T}_{sub}$	Subsurface mean temperature at the bottom of the Ekman layer
UNESCO	United Nations Educational, Scientific and Cultural Organization
UCLA	University of California, Los Angeles
Vpiston	Piston velocity
w'	Anomalous upwelling
$\bar{w}$	Mean upwelling

SUMMARY

Given the strong recent interest in the decadal timescale variability and the potential for its predictability, it is critical to identify dynamics that carry inherent decadal-scale predictability. This work enhances our understanding and prediction capability of the subsurface signature of the decadal variability in the eastern North Pacific upwelling systems using reanalysis products and a set of eddy-resolving ocean model simulations.

We show that subsurface temperature anomalies propagated by mean advection along the North Pacific Current significantly contribute through mean upwelling to decadal changes of surface temperature in the Gulf of Alaska. We also show that this influence is comparable to the contribution associated with variations in atmospheric winds.

We find that subsurface anomalies in the core of the North Pacific Current propagate temperature, salinity, and oxygen signals downstream into the coastal California Current upwelling system, following the path of the mean gyre circulation with a time scale of 10 years. We suggest these propagation dynamics lead to potential predictability of ocean tracers, specifically oxygen and nutrients.

Using reanalysis products and a set of eddy-resolving ocean model simulations, we provide evidence that supports the proposed inherent decadal predictability associated with the propagation of subsurface anomalies. We quantify the predictability of impacts associated with the arrival of the subsurface anomalies in the California Current upwelling system. We find a region of strong deterministic, predictable variance in the core of the North Pacific Current and in the sub-polar gyre region. Finally, we propose a dynamical

subsurface connection between the western and eastern boundary, with subsurface anomalies generating and propagating eastward from the Kuroshio-Oyashio Extension region in the Western Pacific all the way to the California Current region in the Eastern Pacific.

CHAPTER 1.   INTRODUCTION

Pacific Decadal Variability (PDV) plays a critical role, together with the global warming trend, in regulating climate and weather patterns in the Pacific rim countries [e.g., *Liu et al.*, 2012*; Minobe* 1996*; Solomon et al.*, 2011] and marine ecosystems across the Pacific Ocean *[e.g., Di Lorenzo et al.*, 2008*; Mantua et al.*, 1997*; Hare et al.*, 1999*; Miller et al.,* 2004]. Because of the societal impacts of the PDV, identifying the physical mechanisms that control this low-frequency variance for potential decadal predictability has emerged as a new endeavor in climate research [*Meehl et al.*, 2009; 2014; *Mehta et al.*, 2011]. A detailed review of the mechanisms and predictability of the PDV can be found in Liu and Di Lorenzo [2017].

In the North Pacific, a large fraction of surface decadal variability emerges from (1) the reddening of atmospheric variability [e.g., *Hasselman,* 1976] and (2) the westward propagation of large-scale low-frequency Rossby waves. While the first mechanism carries no inherent decadal predictability (i.e., a red noise process), the slow propagation of the Rossby waves towards the western boundary has been exploited for predicting changes in sea level in the Kuroshio Oyashio Extension (KOE) region with timescales between ~2.5-4 years [*Schneider and Miller,* 2001; *Taguchi et al.*, 2007; *Ceballos et al.*, 2009]. These dynamics provide the physical basis for decadal-scale coupling from the eastern to the western boundaries of the North Pacific.

While much of the existing research has explored surface dynamics for decadal predictability of the North Pacific (see review by *Liu and Di Lorenzo*, 2017), fewer studies

explore the role of ocean subsurface dynamics as a source of decadal predictability. Using data from observations and models, several researchers have identified subsurface anomalies in the North Pacific that propagate in the thermocline from their source in subtropical subductions region [*Osafune and Yasuda*, 2013; *Taguchi and Schneider*, 2014; 2017] to the central [*Niklas Schneider*, 2000] and eastern subtropical North Pacific [*Kilpatrick et al.*, 2011; *Sasaki et al.*, 2010]. A recent observational study, using observational Argo data, shows that low-frequency subsurface salinity anomalies propagate from the KOE to the North Pacific Current (NPC) bifurcation region by mean geostrophic advection on timescales of ~7 years [*Kouketsu et al.*, 2017]. Given the coherent nature and slow propagation of anomalies in the subsurface, it is likely that their arrival in the Northeast Pacific impacts the properties of the water masses that feed the upwelling systems of the Gulf of Alaska sub-polar gyre and the California Current eastern boundary current system [*Bograd et al.*, 2015]. Specifically, the upwelling of these anomalies may contribute to the decadal variance of surface physical and biogeochemical quantities such as sea surface temperature and salinity, nitrate and oxygen. Being able to predict decadal changes in these highly productive upwelling systems would have significant societal impact. For example, higher loads of nutrients and lower oxygen concentrations along the California coast are associated with a higher likelihood of hypoxic events (i.e., dead zone) along the U.S. West Coast. Also, higher surface temperature has been linked to the emergence of harmful algal blooms.

The goal of this thesis is to explore the dynamics of subsurface propagation of tracer anomalies in the Northeast Pacific using observations and models, and to quantify the decadal predictability of their impacts in the upwelling systems of the Gulf of Alaska and

California Current System. Specifically, we diagnose the subsurface decadal variability of the North Pacific using an ensemble of historical model hindcasts with the Regional Ocean Modeling System (ROMS) and reanalysis products from 1959-2009.

The examination of the ocean reanalysis products is presented in Chapter 2 and Chapter 3, where we characterize and establish the observational evidence for the propagation of subsurface anomalies by mean advection along the North Pacific Current. We then quantify the impacts of the anomalies as they arrive to the key upwelling systems of the North Pacific, namely the Gulf of Alaska (GOA) and the California Current System (CCS). The chapters are organized around two key questions: (1) How do changes in subsurface circulation and subsurface water properties impact decadal changes in the upwelling systems of the Northeast Pacific? and (2) Can we exploit the subsurface dynamics propagation to predict decadal changes in the upwelling systems?

While results from observational reanalysis in Chapter 2 and Chapter 3 provide evidence that subsurface anomalies carry inherent decadal predictability for the Northeast upwelling systems, quantifying the robustness of these dynamics requires a larger ensemble of realizations. For this reason, Chapter 4 presents a set of ocean modeling experiments designed to quantify the predictability (i.e., deterministic vs. internal variability) associated with the arrival of the subsurface anomalies in the CCS upwelling system. We do so by using an ensemble approach of retrospective ocean simulations and comparisons to reanalysis products for the period 1959-2009. Chapter 4 is organized around the following key questions: (1) How robust are the proposed propagation mechanisms of subsurface anomalies in the North Pacific? and (2) Is the propagation coherent along the entire path from the western to the eastern boundaries?

Finally, Chapter 5 summarizes the thesis, discusses our findings, and outlines directions for future research.

CHAPTER 2.   DECADAL CHANGES IN GULF OF ALASKA UPWELLING SOURCE WATER

2.1   Introduction

Weather patterns and oceanic ecosystems of the North Pacific Ocean are significantly influenced by decadal climate variations. A more thorough understanding of the sources of such low-frequency climate variability is key to improving decadal prediction capabilities [*Barnett et al.*, 1999; *Zhengyu Liu*, 2012; *Z. Liu et al.*, 2002; *N. Schneider et al.*, 2002]. Despite the many promising steps towards decadal prediction, several issues need further exploration such as clarifying the role of the ocean-atmosphere coupling and identifying the processes determining the decadal time scale of climate anomalies [*Latif and Keenlyside*, 2011; *Zhengyu Liu*, 2012]. At low-frequency timescales, previous studies in the North Pacific suggest that subsurface ocean dynamics play an important role in the spreading of low-oxygen waters from the western to the eastern subarctic Pacific [*Whitney et al.,* 2007]. Given the low-frequency timescales of subsurface dynamics, the purpose of this work is to understand the role of subsurface temperature anomalies in the generation of decadal SST variability in the Northeast Pacific. Specifically, we focus on the Gulf of Alaska (GOA), one of the most productive ecosystems in the North Pacific Ocean. Here

the upwelling of subsurface anomalies will be shown to contribute significantly to the GOA decadal fluctuations, which are linked to important changes in marine ecosystems.

Decadal changes in the SST of the Gulf of Alaska are linked to the Pacific Decadal Oscillation (PDO), the leading mode of SST variability in the North Pacific [*Mantua et al.*, 1997; *N. Schneider and Cornuelle*, 2005]. The PDO is forced predominantly by the surface expression of the Pacific North American (PNA) pattern [*Wallace and Gutzler*, 1981], which is reflected in the position and the strength of Aleutian Low sea-level pressure over the GOA.

Using a simple stochastic climate model, proposed by *Hasselmann* [1976], Cummins and Lagerloef [2002] demonstrated that a large fraction of the SST low-frequency variability in the GOA can be reconstructed by Ekman pumping dynamics. Their model equation follows:

$$\frac{dSSTa}{dt} = w'\bar{T}_{sub} - \frac{SSTa}{\tau} \, , \qquad (1)$$

where changes in SST anomalies (SSTa) over the depth of the Ekman layer are driven by anomalous upwelling (w') acting on the mean temperature at the bottom of the layer ($\bar{T}_{sub}$). The second term on the right-hand side of Eq. 1 is associated with the damping of SSTa over the timescale (τ). When applying this local Markov model (Eq. 1), *Cummins and Lagerloef* [2002] estimated changes in Ekman velocity using a reanalysis of winds over the GOA. The damping timescale can be estimated by computing the average temporal decorrelation timescale of observed SSTa in the GOA (~4-6 months) [e.g., *Chhak et al.*, 2009].

Although the Ekman process model (Eq. 1) exhibits a strong capability of reconstructing the GOA SSTa, this model does not consider SSTa contributions associated with the mean upwelling of subsurface temperature anomalies generated by gyre-scale circulation dynamics. This study expands the Ekman process model of *Cummins and Lagerloef* [2002] to include the contributions of the mean upwelling ($\overline{w}$) acting on subsurface temperature anomalies at the base of the Ekman layer (T'_{sub}) as follows:

$$\frac{dSSTa}{dt} = \; w'\overline{T}_{sub} + \overline{w}T'_{sub} - \frac{SSTa}{\tau}. \tag{2}$$

In particular, we seek to understand how changes in subsurface circulation and water properties impact the Gulf of Alaska and quantify their contribution to surface low-frequency variability.

The remainder of this chapter is structured as follows. Section 2.2 presents the data and the isopycnal analyses. Section 2.3 describes the results of the propagation of subsurface temperature anomalies along the North Pacific Gyre in the Gulf of Alaska region and validates this propagation pattern with an observational dataset. Section 4 investigates the role of subsurface anomalies in the sea surface temperature of the GOA and Section 5 summarizes and concludes this chapter.

2.2 Data and Methods

We investigate the subsurface temperature anomaly using two observational reanalysis datasets. The first is the European Centre for Medium-range Weather Forecasting (ECMWF) Ocean Reanalysis System (ORA-S3). This dataset has a horizontal resolution

of 1° x 1° in longitudinal and latitudinal directions, respectively, and 29 vertical levels spanning the period from January 1959 to December 2009 [*Balmaseda et al.*, 2008]. The second reanalysis dataset is the Simple Ocean Data Assimilation (SODA 2.1.6). The spatial horizontal resolution of the SODA output is 0.5° x 0.5° with 40 vertical levels covering the period from January 1958 to December 2008 [*Carton and Giese*, 2008].

To explore the role of the gyre-scale circulation in generating subsurface anomalies in the GOA, we perform an isopycnal (constant-density surface) analysis. To calculate the density field, we use the SODA and ORA-S3 monthly temperature and salinity fields and follow the UNESCO International Equation of State [*Unesco*, 1983]. The monthly density of each vertical level is linearly interpolated onto isopycnal surfaces using the transformation from the z-coordinate to sigma-coordinate systems, a method described in *Chu et al.* [2002]. We use the temperature anomalies on isopycnal $\sigma_\theta = 26.5$ kg m^{-3} as a proxy for subsurface temperatures that feed the GOA upwelling. This isopycnal layer does not outcrop during the winter months in either reanalysis product in the Northeast Pacific, allowing us to track changes in the properties of water masses associated with gyre-scale circulation. The 26.5 isopycnal layer is ventilated in the western subarctic Pacific, where the imprint of surface properties is transferred from the mixed layer to the ocean interior, and exchanges gases with the atmosphere. Surface processes affect this isopycnal through vertical mixing upstream of the North Pacific Gyre in the Kuroshio-Oyashio Extension (KOE) region.

To track subsurface low-frequency variance, we use temperature anomalies on isopycnal $\sigma_\theta = 26.5$ kg m^{-3}. Since temperature and salinity anomalies are compensated on a given isopycnal surface (warm/salty or cool/fresh water masses) [*Veronis*, 1972], temperature anomalies can be considered either isopycnal spiciness or salinity anomalies. We calculate

the temperature anomalies of isopycnal layers by removing the monthly average and the trend from the temperature field. In addition, we compute the global average stream function based on Bernoulli's Law, assuming that the density of the layer is constant along the streamline and then integrating the pressure of a column of water above each point on the isopycnal layer.

Although long-term observations of subsurface variability are rare, we use an observational data set of temperature observations on isopycnal layer $\sigma_\theta = 26.5\ kg\ m^{-3}$ from Ocean Station PAPA (P26 or OSP), located at 145°W and 50°N from August 1956 to February 2006 [*Whitney et al.*, 2007]. The spatial and temporal resolutions of the OSP archive allow a description of not only the mean state but also the variability in the main state of the ocean in the Gulf of Alaska [*Freeland*, 2007]. A detailed description of the history of OSP salinity sampling is presented in *W Crawford et al.* [2007].

The sources of the SST and SLP data are the National Oceanic and Atmospheric Administration (NOAA) Extended Reconstructed SST analysis [*Smith and Reynolds*, 2003; 2004; *Smith et al.*, 2008] and the National Centers for Environmental Prediction-National Center for Atmospheric Research (NCEP/NCAR) project [*Kalnay et al.*, 1996], respectively.

We estimate the significance of the correlation coefficient using a Monte Carlo technique. In this approach, each time series is approximated as an auto-regressive order 1 model (AR-1) with the same lag-1 correlation coefficient computed from the original time series. We use the AR-1 models to generate 5,000 realizations of two random red-noise time series and then compute the probability distribution function (PDF) of their cross-correlation

coefficients. The final significance level is inferred from the correlation value associated with the 95% area under the PDF. Throughout this text, we will denote correlation coefficients by R.

2.3 Subsurface propagation of anomalies along the gyre in the GOA

To characterize subsurface circulation and anomalies in the GOA, we defined a subsurface index for the Gulf of Alaska region, the Gulf of Alaska subsurface index (GOAsub index). This index consists of spatially-averaged subsurface temperature anomalies in the isopycnal 26.5 layer in the region defined by coordinates 152.5°W – 142.75°W and 55.30°N – 59.00°N (Figure 1b, black square). Figure1a shows the evolution in time of the SODA (dashed gray line) and ORA-S3 (solid black line) GOAsub indexes. Although the indexes show differences in year-to-year variability, (e.g., 1965, 1968, 1990, and 2000), both time series have the same tendency and a low-frequency component. The low-frequency timescale of the GOAsub indexes is determined by double integration effects associated with the geostrophic advection of anomalies in the subsurface by the gyre circulation dynamic [*Kilpatrick et al.*, 2011; *Di Lorenzo and Ohman*, 2013]. The ORA-S3 GOAsub index is smoother while the SODA GOAsub index is noisier. Because of the high resolution of the SODA database, the noise in the results occurs mostly in the high frequency. Therefore, both indexes are correlated by a factor of 0.6 at a >99% confidence level. The spatial correlation map between the index and the ORA-S3 subsurface temperature anomalies on the isopycnal 26.5 is above 0.8 in the region of the GOA (Figure 1b). The SODA correlation maps (not shown) are very similar to the ORA-S3 but exhibit more noise in space. Given our interest in understanding the large-scale and low-frequency

components of the subsurface temperature signal, we have selected the coarser resolution

ORA-S3 maps to present the subsurface analyses.
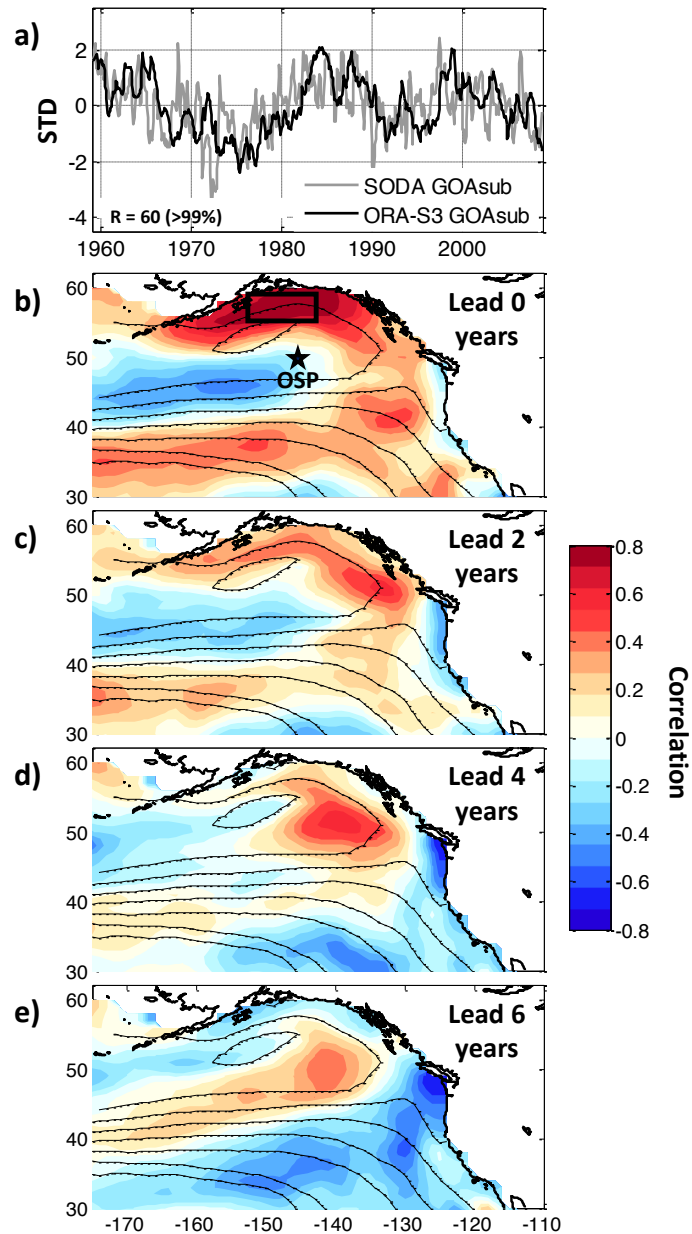
Figure 1. (a) Time series of the SODA (gray, dashed line) and ORA-S3 (black, solid line) GOAsub indexes from 1958 to 2010. Lead correlation maps between the salinity field on the $\sigma_0 = 26.5$ kg m^{-3} isopycnal and the ORA-S3 GOAsub index at (b) lead 0 years

The temporal evolution of the GOAsub signal in the subsurface is characterized using lead/lag correlation maps between the GOAsub index at year 0 and the isopycnal temperature anomalies during previous years (e.g., lead 0, 2, 4, and 6 years) in Figure 1b-e. The figure shows that during previous lead times, a signal of this correlation propagates with the mean circulation. At lead 0 years, the maximum correlation between the GOAsub index and the subsurface temperature anomalies on the isopycnal 26.5 (R = 0.8) is in the Northern GOA in the region where the index was defined (Figure 1b). At lead 2 years (Figure 1c), the peak correlation has shifted upstream of the Alaskan Gyre along the coast of British Columbia. At lead 4 years, the peak correlation has shifted further to the south of the Northern GOA. At lead 6 years, the southwest backward propagation of the GOAsub signal along the mean gyre circulation becomes even more evident. By lead years 4 and 6, the signal, now weaker (R = 0.4-0.6), has moved away from the Northern GOA and stretches along the axis of the North Pacific Current. At lead 8 years, the signal weakens (R = 0.2) (not shown) and is centered at 150°W and 45°N. The same analysis conducted for future lag times shows the Northern GOA subsurface signal stretching and disappearing along the Aleutians (not shown), consistent with the Alaskan Gyre circulation.

The same analysis is performed with the SODA dataset (not shown), which reveals similar propagation patterns. A weak signal in the southwest GOA region that propagates following circulation reaches the GOA region at lag 0 and stretches at later lag times. The main difference is that the signal is noisier in SODA.

To check the consistency of the reanalysis products in capturing subsurface signals, we compare a time series of subsurface temperature anomalies from the ORA-S3 dataset with *in situ* subsurface observations at Station PAPA (OSP). The temperature anomalies in the

12

OSP are used to build an index, Station PAPA, or the SP index. Figure 2 shows the time series of the observed (purple line) and ORA-S3 (light blue line) SP indexes, both of which are correlated by a correlation factor of 0.74 (>99% of confidence). Until 1980, both indexes evolved almost simultaneously, with two large anomalous values recorded in 1961 and 1975. Between 1980 and 1995, the SP index exhibits differences between the two datasets, and afterwards, the anomalies exhibit the same trend in both indexes. The propagation of temperature anomalies along the mean gyre circulation, shown in the correlation map analysis between the ORA-S3 GOAsub index and the temperature anomalies on the $\sigma_\theta = 26.5 \ kg \ m^{-3}$ isopycnal (Figure 1), were found to be consistent with the propagation of anomalies inferred from lead/lag correlation maps between the ORA-S3 SP index and the temperature anomalies on the same isopycnal layer (not shown in figures).
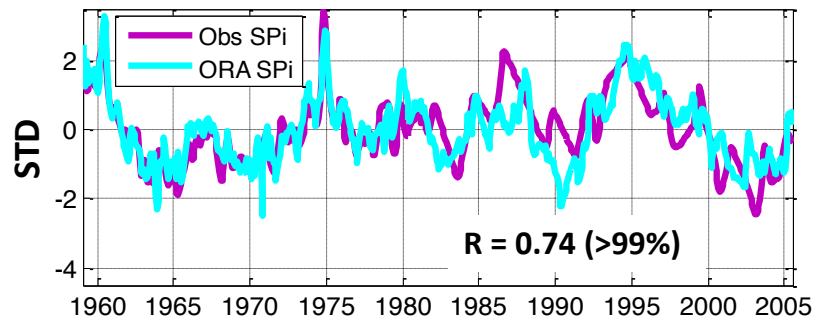
Figure 2. (a) Time series of the salinity anomalies from Station PAPA (Obs SP index) (purple line) and from the ORA-S3 dataset (ORA SP index) (light blue line) from 1959 to 2005 (correlation R = 0.74, >99% confidence).

2.4   The role of GOA subsurface anomalies in surface temperature

To explore the role of subsurface anomalies in modulating low-frequency SSTa in the GOA, we expand the Ekman pumping model of *Cummins and Lagerloef* [2002] by suggesting that variability in upper-ocean temperature anomalies in the GOA is driven by changes in both upwelling velocity, resulting from wind anomalies, and the subsurface water mass properties. We therefore propose the model described in Eq. 2 for the low-frequency SSTa in the GOA.

We test the expanded Ekman process model (Equation 2) in a control volume over the GOA (red box in Figure 3a), where we define the index of SST anomalies (GOA-SSTa index) (red line in Figure 3b) as the average of monthly SST anomalies extracted from the NOAA from 1950 to 2011. Figure 3a shows the correlation map of this index and SST anomalies in the Gulf of Alaska. This correlation pattern reproduces the spatial signature of the PDO: the negative values of SST anomalies in the Central North Pacific and positive values along the West Coast and in the Gulf of Alaska [*Mantua et al.*, 1997]. This pattern is also evident by the significant correlation between the time series of the GOA-SSTa and PDO indexes (Figure 3b).

To recover the *Cummins and Lagerloef* [2002] model, we define an index of wind-induced Ekman pumping (w') using sea level pressure anomalies (SLPa) over the GOA. The goal is to define a w' index that is optimal in capturing SSTa variability so that we can quantify how much of the SSTa variability can be explained by surface atmospheric forcing vs. how much is driven by subsurface processes. First, we compute a regression map of the SLPa on the GOA-SSTa index (Figure 3b) to isolate the optimal spatial pattern of atmospheric

14

forcing. Consistent with previous findings [*Chhak et al.*, 2009], the atmospheric forcing pattern of GOA-SSTa shows the predominant signature of the Aleutian low, characterized by basin-scale negative SLP anomalies between 20°N and 60°N. This characteristic SLP anomaly pattern in the GOA defines the best pattern of the atmospheric forcing of SST anomalies. We now use this pattern to build an index for the atmospheric forcing of the SST by projecting the SLPa field onto the pattern. This projection operation yields the SLPa index. This approach ensures that the SLPa index captures most of the atmospheric-induced variability of SSTa. A correlation between the raw monthly SLPa index and the GOA-SSTa index exhibits a significant correlation of 0.21 (a >99% significance level) (Figure 3d, dark green and red lines, respectively).
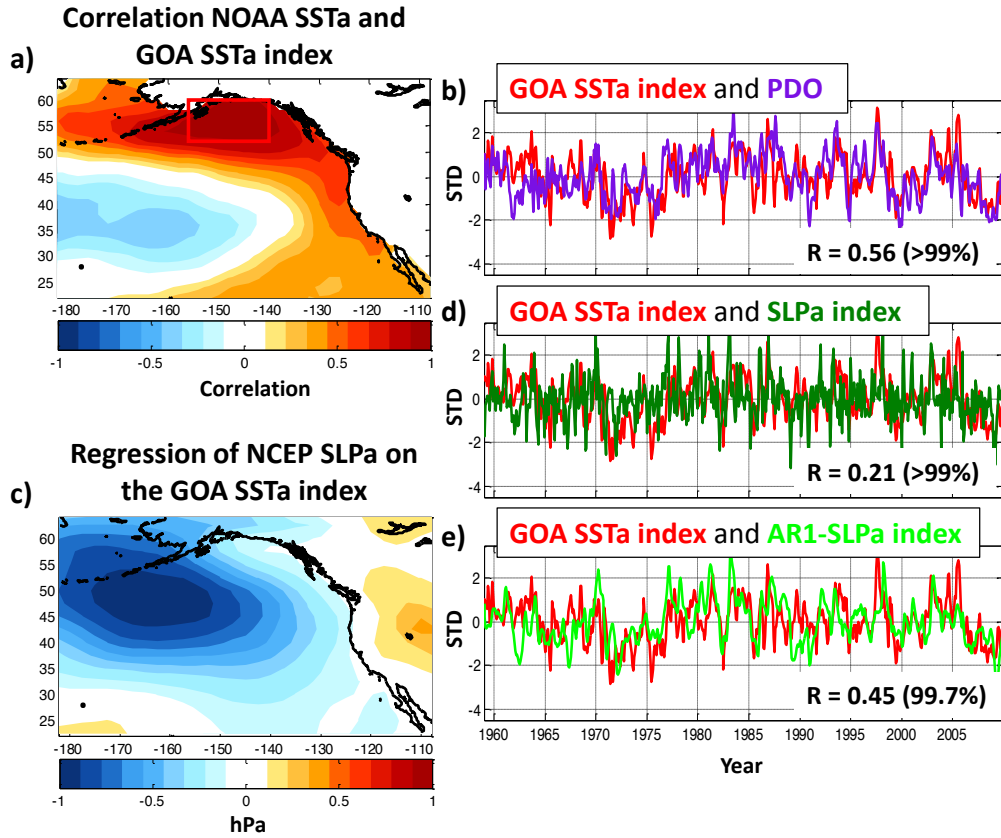
Figure 3. (a) Correlation map between SST anomalies and the GOA-SSTa index. The latter is the average temperature anomaly in the region of the red box. (b) Time series of the GOA-SSTa index (red line) compared to the PDO index (purple line) from 1959 to 2009 (correlation R = 0.56, >99% significance). (c) Regression of SLPa on the GOA SSTa index. (d) Time series of the GOA-SSTa index (red line) compared to the SLPa index (dark green line) (correlation R = 0.21, >99% significance). (e) The GOA-SSTa index (red line) compared to the SLPa index (light green line) from the AR1-model (correlation R=0.45, 99.7% significance).

Neglecting the subsurface mean upwelling term ($\overline{w}$ in Eq.2) acting on the subsurface anomalies (T'_{sub}), we recover the model of *Cummins and Lagerloef* [2002] (Eq.1), which is equivalent to an auto-regressive model of order 1 (AR-1). To reconstruct GOA-SSTa index variability driven by atmospheric forcing, we take the SLPa index as a proxy of atmospheric forcing, using it as the forcing function in the AR-1 model. Because SLPa are correlated with changes in heat fluxes over the GOA, the SLPa forcing function contains

16

the effects of both direct Ekman pumping and surface heating over the SSTa. Given that the effects of both Ekman pumping and surface heating can be represented as an AR-1 model, we refer to the AR-1 model hindcast as the fraction of variability in SSTa driven by atmospheric forcing. In the AR-1 model, SSTa damping scale τ, computed from the autocorrelation timescale of the GOA-SSTa index, is set to six months. This value of the damping scale is consistent with that of previous studies (e.g., *Chhak et al.* [2009]). By selecting a longer timescale for damping (e.g., 12-18 months), as in *Cummins and Lagerloef* [2002], we obtain similar results with a smoother SSTa time series. To solve the AR-1 model, we use a simple Euler forward time step scheme. The AR-1 model forced by the SLP anomalies (AR1-SLP index, the light green line in Figure 3e) filters the high-frequency component associated with atmospheric forcing and produces a signal characterized by stronger low frequency [*Rudnick and Davis*, 2003]. Using this reconstruction, we observe that the variance of the SST explained by atmospheric forcing increases significantly (R = 0.45, a 99.7% significance level). To estimate the contribution of the surface forcing to the low-frequency variance of the SSTa, we apply a six-year low-pass filter to the AR1-SLPa index (Figure 4a). The correlation between the six-year filtered GOA-SSTa and the AR1-SLPa index has a low statistical significance (R = 0.55, an 85.2% significance level, Figure 4a), suggesting that other processes in addition to Ekman pumping and surface heating (atmospheric forcing) contribute to the decadal variance of the SST in the GOA.

We now explore the contributions of the mean upwelling of subsurface anomalies to SSTa variability using Eq. 2. We use the GOAsub index (Figure 1) as a proxy for variability driven by the subsurface anomalies ($\overline{w}T'_{sub}$). Given that the GOAsub index is already

dominated by low-frequency variability, the integration of Eq. 2 does not change the character of the GOAsub index. Therefore, to quantify the contributions of GOAsub to the decadal variations of the SSTa, we simply apply a six-year low-pass filter to the GOAsub (Figure 4b). The results suggest that subsurface anomalies flowing upward by the mean upwelling explain an equal fraction of the decadal variability of the SST (R=0.51) when compared to that of the surface Ekman pumping in the Gulf of Alaska region (R=0.55) (compare Figures 4a and 4b). To examine the degree to which these surface and subsurface forcings of the SSTa are independent, Figure 4c shows the low-pass GOA-sub and AR1-SLPa index time series and their correlation coefficient. The low correlation (R = 0.16, a 31% significance level) between these two indexes shows that atmospheric forcing (anomalous upwelling velocity) and subsurface forcing (temperature anomalies on the isopycnal 26.5) are largely independent, indicating that each forcing captures a different aspect of the low-frequency variance of the SST. Since atmospheric and subsurface forcings are independent, they can be combined in a linear model for the SSTa in the Gulf of Alaska,

$$SSTa(t) = \alpha(AF) + \beta(SF), \tag{3}$$

where AF is atmospheric forcing (anomalous upwelling velocity), represented as the AR1-SLPa index, and SF is subsurface forcing (subsurface temperature anomalies on the isopycnal 26.5 advected by the mean upwelling), represented as the GOAsub index. Parameters $\alpha = 0.39$ and $\beta = 0.29$ are obtained using least squares. Figure 4d shows the results of the low-pass filter linear model (Eq. 3) for the GOA-SSTa (Figure 4d blue line) and GOA-SSTa indexes (Figure 4d red line). The low-pass filter is shown to highlight the

decadal variance of the indexes. The correlation factor without a filter applied (not shown) is R = 0.53 (a >99% significance level) and with a six-year filter applied is R = 0.70 (a 97.4% significance level). These results indicate that the linear model proposed here and forced by Ekman pumping and subsurface temperature anomalies explains almost half of the low-frequency variance of the SST in the GOA.
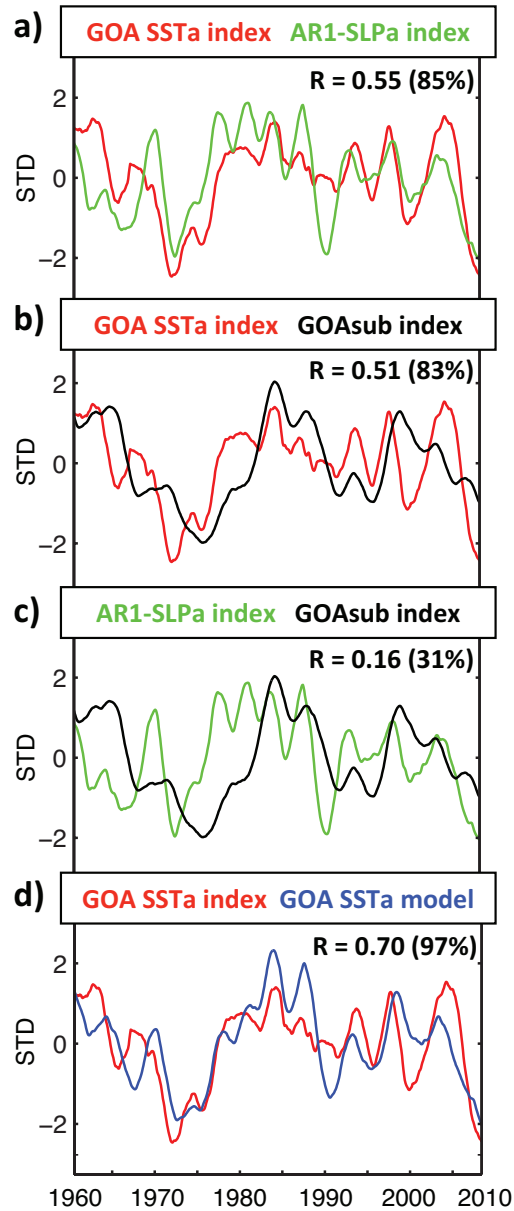
Figure 4. Six-year low-pass filtered times series of (a) the GOA-SSTa index (red line) compared to the AR1-SLPa index (green line) (correlation R = 0.55, 85.2% significance); (b) the GOAsub index (black line) compared to the GOA-SSTa index (red line) (correlation R = 0.51, 83% significance); (c) the GOAsub index (black line) compared to the AR1-SLPa index (green line) (correlation R = 0.16, 31.1% significance); and (d) the GOA-SSTa index (red line) compared to the GOA-SSTa index modeled by Eq. 2 (blue line) (correlation R = 0.70, 97.4% significance).

2.5   Discussion and Conclusion

This study examined the role of subsurface temperature anomalies on the isopycnal layer $\sigma_\theta = 26.5 \ kg \ m^{-3}$ in modulating the low-frequency variability of the SST in the GOA. The results reveal that temperature anomalies advected in the subsurface by the gyre-scale circulation exhibit significant low-frequency variability and contribute through mean upwelling to an important fraction of decadal variance of SST in the GOA upwelling system. Advected by the mean circulation, these subsurface anomalies are tracked back into the North Pacific Current. The dynamics generating the subsurface anomalies remain unclear.

Previous studies suggest that these subsurface anomalies along the axis of the North Pacific Current could be initiated by surface buoyancy forcing [*Nonaka and Xie*, 2000] and by anomalous advection upstream of the subtropical subduction regions in the Kuroshio-Oyashio Extension (KOE) region [*Taguchi and Schneider*, 2014]. Once these subsurface anomalies are generated in their source regions, they are advected by the main geostrophic current towards the eastern Pacific. Using a conservative water-mass tracer along isopycnals, *Whitney et al.* [2007] reported a propagation of oxygen anomalies from the KOE region eastward across the Pacific. The present study shows how temperature anomalies reach also the subarctic gyre and the GOA, where they mixed into the upper ocean through upwelling. However, it remains unclear if and how much the subsurface anomalies are attenuated during the course of their propagation from the KOE to GOA regions, or if other processes contribute to generation of subsurface anomalies along the axis of the gyre in the central and eastern North Pacific.

While future studies should identify the dynamics underlying the initiation and attenuation of these anomalies along their propagation path, this study suggests that tracking the propagation of subsurface anomalies may enhance our ability to make decadal predictions of surface variability in the Gulf of Alaska and the PDO pattern. By identifying the role of the advected subsurface anomalies generated along the North Pacific Current, this work contributes to our understanding of the mechanisms/sources of decadal variability in the Gulf of Alaska and its impact on local marine ecosystems. Given the exceptional low-frequency character of the propagation of subsurface anomalies along the gyre, future study should conduct long-term, high-resolution ocean model simulations to further diagnose the processes generating the anomalies and how robust are the decadal predictions.

CHAPTER 3. DECADAL DYNAMICS AND PREDICTABILITY OF OXIGEN AND SUBSURFACE TRACERS IN THE CALIFORNIA CURRENT SYSTEM

3.1   Introduction

Coastal ocean hypoxia has emerged as a growing threat to marine ecosystems and fisheries, and raises concerns for human health [*Diaz and Rosenberg*, 2008; *McClatchie et al.*, 2010; *Rabalais et al.*, 2010]. In the California Current System (CCS), like most other coastal ocean upwelling systems, changes in the oxygen content are controlled by complex interactions between circulation and biogeochemistry, and show prominent fluctuations on interannual and decadal timescales [*Bograd et al.*, 2008; *Crawford and Pena*, 2016; *Deutsch et al.*, 2006, *Deutsch et al.*, 2011].

Over the shelf region where the marine ecosystem is most sensitive to hypoxia, changes in oxygen are strongly controlled by coastal upwelling [*Bograd et al.*, 2008; *Chan et al.*, 2008; *Connolly et al.*, 2010]. Vertical fluxes of nutrient-rich subsurface waters to the surface can trigger high production of new organic matter on the shelf. As the organic matter sinks, bacterial decomposition in the subsurface depletes oxygen leading to hypoxic events [*Chan et al.*, 2008; *Grantham et al.*, 2004].

While wind-induced upwelling and biological processes drive the interannual variability of the oxygen content on the shelf [*Checkley and Barth*, 2009; *Connolly et al.*, 2010; *Peterson et al.*, 2013], it has been recognized that long-term changes in the oxygen content of the CCS source waters for the coastal upwelling are equally important [*Bograd et al.*, 2015] and may influence the statistics of coastal hypoxia. This latter process is summarized in the idealized cross-shore vertical model of coastal upwelling in schematic Figure 5. This model illustrates how the pool of subsurface water masses (the green shadow region) contributes to the oxygen content in the shelf (the red shadow region) through mean upwelling (gray arrows).
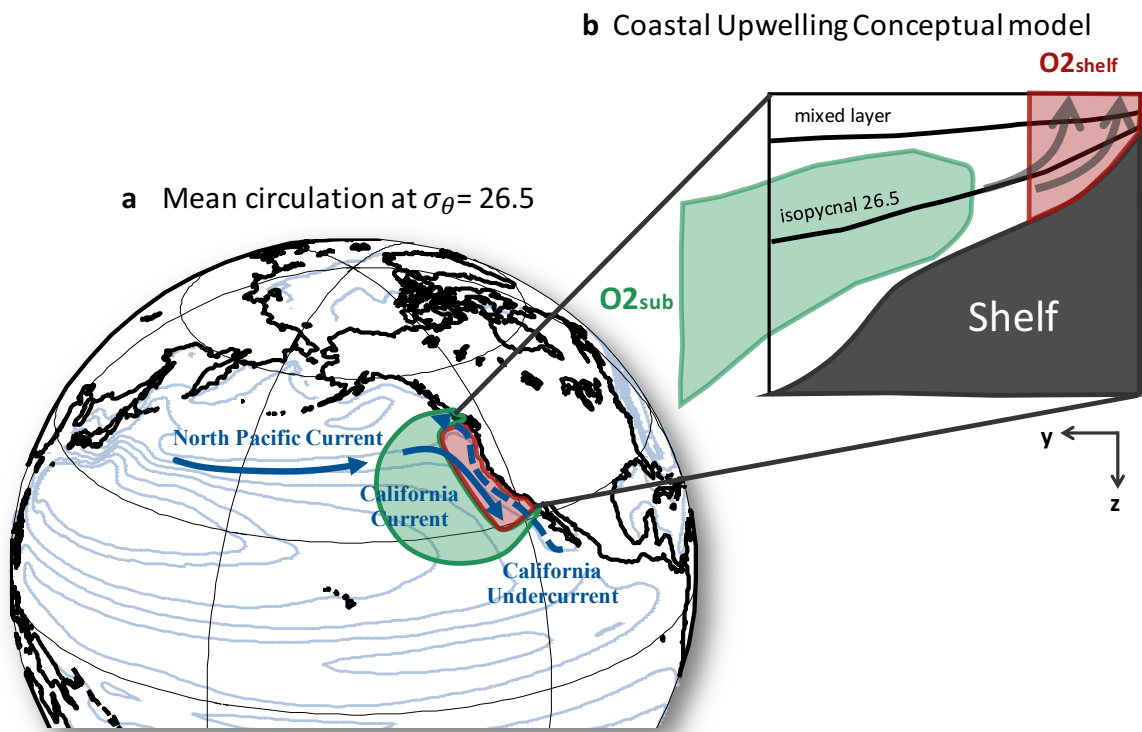
Figure 5. Conceptual model of water masses upwelling in the CCS. (a) Contours represent the ORA-S3 mean Bernoulli's stream function along isopycnal 26.5 from 1959 to 2010 showing the path of the mean subsurface circulation. Blue arrows represent the major currents that converge in the CCS region: North Pacific Current, California Current, and California Undercurrent. (b) Idealized cross-shore vertical

profile of the shelf to illustrate large-scale subsurface dynamics impacting oxygen in shelf coastal waters. The pool of subsurface waters (green shadow region) feed the main upwelling (gray arrows) and impact the control volume of oxygen content in the shelf (red shadow region).

Below the mixed layer, oxygen anomalies on the shelf of the southern CCS have undergone a large decline (approximately a 20%) over the last three decades [*Bograd et al.*, 2008] (Figure 6a, red line from 1980 to 2012). Similar declining oxygen values have been reported over the continental shelf of the northern CCS [*Peterson et al.*, 2013] (Figure 6a, orange line from 1998 to 2012). *Meinvielle and Johnson* [2013] find similar declining trends all along the continental shelf break between 25° to 50°N with a maximum near the core of the CUC. While these drops in oxygen values exhibit the longest and the strongest negative trend in the observed oxygen time series over the CCS, an extension of the time series to 1950 in the southern CCS [*Koslow et al.*, 2011] (Figure 6a, red line) and to 1960 in the northern CCS [*Pierce et al.*, 2012] (Figure 6a, orange line) shows that this trend is neither monotonic [*McClatchie et al.*, 2010] nor significant [*Koslow et al.*, 2011]. Therefore, the observed oxygen variability is best characterized in terms of multi-decadal fluctuations rather than a negative trend [*Bograd et al.*, 2008; *Meinvielle and Johnson*, 2013; *Pierce et al.*, 2012; *Whitney et al.*, 2007]. Additional analysis of the CCS oxygen data [*Deutsch et al.*, 2011] (Figure 6a, green line) confirms that the variability of oxygen anomalies in the CCS is strongly modulated by a multi-decadal oscillation [*Deutsch et al.*, 2011]. This type of decadal variability is also reported in a recent study [*W R Crawford and Pena*, 2016] showing a significant dome-shaped temporal pattern of subsurface oxygen in the CalCOFI region. In the subsurface, tracers like oxygen, salinity, and temperature are expected to have a predominant multi-decadal timescale because of the long-term memory of the ocean and of "double integration" effects [*Di Lorenzo and Ohman*, 2013; *Ito and*

Deutsch, 2010; *Kilpatrick et al.*, 2011]. In the subsurface, ocean tracers integrate the variability associated with geostrophic currents, which are already the result of an integration of the surface atmospheric forcing. These double integration effects lead to a very strong reddening (i.e., amplification of low frequency variance) of the tracers' spectrum.
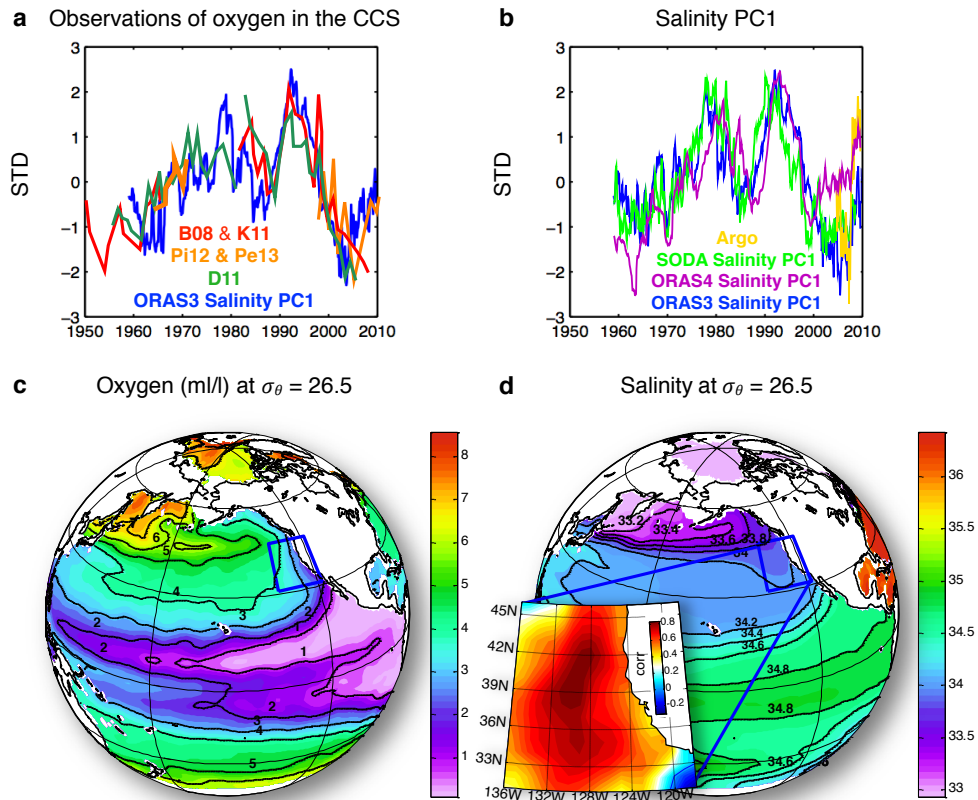
Figure 6. Low-frequency variability of the subsurface oxygen content (oxygen content on the 26.5 kg m^{-3} isopycnal surface) in the CCS. a, Time series of the observed oxygen along the West Coast of North America: *Bograd et al.* **[2008] and** *Koslow et al.* **[2011] (B08 and K11; red line);** *Pierce et al.* **[2012] and** *Peterson et al.* **[2013] (Pi12 and Pe13; orange line);** *Deutsch et al.* **[2011] (D11; green line); and ORA-S3 salinity leading pattern or principal component (PC1; blue line). The ORA-S3 salinity PC1 (blue line) is computed from normalized salinity anomalies on the isopycnal 26.5 in the region of the blue box in c and d. b,** Time series of the PC1 of salinity for ORA-S3 (blue line, same as in a), ORA-S4 (purple line), SODA 2.1.6 (green line), and Argo mean salinity anomalies (yellow line) on the region of the PC1 (blue square in d). **c,** Annual mean

dissolved oxygen distribution (ml/l) and d, salinity (psu) along the isopycnal 26.5 kg m^{-3} on the Pacific Ocean from the World Ocean Database 2013 [*Boyer et al.,* 2013]. The spatial pattern of the salinity PC1 is shown as a pop-up of the CCS region. The units for the colorbar of the pop-up are correlations between PC1 and salinity anomalies on the isopycnal 26.5.

Previous studies have explored the role of large-scale climate processes such as the Pacific Decadal Oscillation (PDO) and North Pacific Gyre Oscillation (NPGO) [*Deutsch et al.,* 2011; *Di Lorenzo et al.,* 2008; *Peterson et al.,* 2013] as generating mechanisms for the low-frequency fluctuations of oxygen in the CCS. While climate modes like PDO and NPGO share correlation with the full-length oxygen CalCOFI time series of *Koslow et al.* [2011] with values of R~0.4, this correlation is higher in the summer when the climate modes are weak and is not statistically significant if we account for the large auto-correlation in the oxygen data. Given that PDO and NPGO are defined using sea surface temperature [*Mantua et al.,* 1997] and height [*Di Lorenzo et al.,* 2008], the modes capture variability confined in the upper ocean (e.g., 0-150m) [*Chhak et al.,* 2009] and are not necessarily good indicators of the oxygen subsurface dynamics.

In the thermocline, large-scale horizontal circulation plays an important role in modulating the variability of subsurface water properties in the eastern North Pacific [*Chikamoto et al.,* 2015; *Kilpatrick et al.,* 2011], Gulf of Alaska [*Pozo Buil and Di Lorenzo,* 2015], and CCS [*Bograd et al.,* 2015; *Peterson et al.,* 2013]. Zonal subsurface advection from the North Pacific gyre into the CCS draws young water masses characterized by high oxygen (Figure 2c) and low nutrient concentration [*Hickey,* 1979; *Lynn and Simpson,* 1987]. These source waters also transport the low salinity signature from ventilated thermocline waters (Figure 2d) in the western Pacific [*Hickey,* 1979]. From the south, the California Undercurrent (CU) transports along the upper continental slope old, salty, and oxygen-

depleted waters from the tropical oxygen minimum zones (OMZ) [*Gay and Chereskin*, 2009; *Lynn and Simpson*, 1987; *Wyrtki*, 1962] (Figures 6c, d), where the weak ocean ventilation and biogeochemical transformations maintain low oxygen levels [*Bograd et al.*, 2008; *Hickey*, 1979; *Stramma et al.*, 2010], to all the way to Alaska [*Thomson and Krassovski*, 2010].

In this study, we hypothesize that decadal changes in the oxygen content of the CCS upwelling source waters are primarily controlled by the transport of subsurface water mass anomalies associated with the mean gyre-scale circulation (i.e., mean advection of subsurface water mass anomalies). Diagnosing the decadal dynamics of subsurface oxygen is complicated given the lack of spatially and temporally resolved oxygen observations. However, to the extent that biological controls play a minor role in the multi-decadal variability of subsurface oxygen (e.g., *Deutsch et al.* [2006]), changes in oxygen should be correlated with physical tracers like salinity and temperature on isopycnal layers, which are better sampled spatially and temporally. The goal of this chapter is to show that long-term oxygen variability recorded in the California Current System has a predominant subsurface physical control associated with the decadal propagation of water mass anomalies transported by the gyre-scale circulation, which is inherently predictable.

The remainder of the Chapter 3 is organized as follows. Section 3.2 describes the data and the methodology used in this study. Section 3.3 introduces a salinity-based physical proxy for subsurface oxygen and its validation with observational long-term data along the CCS. Section 3.4 uses the salinity-based physical proxy to investigate the physical controls of multi-decadal oxygen variability. A summary and discussion of the implications for

decadal predictability of oxygen of the CCS upwelling source waters are provided in Section 3.5.

3.2   Data and Methods

The reference time series for the observed multi-decadal variability of oxygen in the CCS (Figure 6a) are taken from previous published work [*Bograd et al.*, 2008; *Deutsch et al.*, 2011; *Koslow et al.*, 2011; *Peterson et al.*, 2013; *Pierce et al.*, 2012] and cover the period 1950-2010. These time series are developed using different analyses of subsurface oxygen from the CalCOFI hydropgrahy [*Bograd et al.*, 2008; *Deutsch et al.*, 2011; *Koslow et al.*, 2011] and data collected in the Oregon Shelf [*Peterson et al.*, 2013; *Pierce et al.*, 2012]. For the purpose of computing correlations with the CCS oxygen time series we use the CalCOFI portion of the data updated by Koslow and Bograd (personal communication), which has more temporal coverage.

To explore the physical control of subsurface oxygen we focus our analysis on the $\sigma_\theta = 26.5\ kg\ m^{-3}$ isopycnal surface, which ventilates in the western subarctic Pacific and does not outcrop in CCS during winter. To perform the isopycnal analysis we use primarily salinity and temperature data from the European Centre for Medium-range Weather, Forecasting (ECMWF) Ocean Reanalysis System (ORA-S3) [*Balmaseda et al.*, 2008] over the period 1959-2009. Results obtained from the ORA-S3 analysis are also compared to the Simple Ocean Data Assimilation (SODA; version 2.1.6) [*Carton and Giese*, 2008], the ECMWF ORA-S4 [*Balmaseda et al.*, 2013] and available gridded Argo observations. Using the monthly temperature and salinity fields, we calculate the potential density field for each vertical level according to the United Nations Educational, Scientific and Cultural

Organization International Equation of State [*Unesco*, 1983]. Then fields are linearly interpolated onto isopycnal surfaces using the transformation from z-coordinates to sigma-coordinate system method [*Chu et al.*, 2002]. We use the same approach for all reanalysis and Argo products.

To define the mean gyre-scale circulation along the $26.5 \ kg \ m^{-3}$ isopycnal surface we compute the Bernoulli stream function assuming constant density along streamlines and then integrating the pressure of a column of water above each point on the isopycnal layer.

Here we estimate the significance of the correlation coefficients (R) between two time series by using a Monte Carlo method. In this approach, each time series is approximated as a first-order auto-regressive (AR-1) model with the same autoregression coefficient computed from the original time series. We use the AR-1 models to simulate 5,000 realizations of two random red-noise time series. The final percent significance is then determined based on the probability distribution function (PDF) of the cross-correlation coefficients between the two timeseries.

3.3   Physical controls of multi-decadal oxygen variability

To test the extent to which multi-decadal variability in the oxygen source waters of the CCS upwelling is primarily controlled by changes in the physical dynamics, we compare the available observed oxygen time series to the variability of a subsurface passive tracer such as salinity on a constant density surface ($\sigma_\theta = 26.5 \ kg \ m^{-3}$) located below the ocean mixed layer. The choice of salinity is motivated by the high spatial correlation of the annual mean salinity and dissolved oxygen concentration in the North Pacific (Figure 6c and 2d, high salinity → low oxygen). To characterize the subsurface physical variability,

we extract the leading Empirical Orthogonal Function (EOF1) of the salinity anomalies on the isopycnal 26.5 in the CCS region defined by coordinates 136°W – 118°W and 31°N – 46.5°N (Figure 6d, blue square). The time series of this leading pattern or principal component (PC1, Figure 6a, blue line) inferred from ECMWF ORA-S3 is compared to the available oxygen observations (Figure 6a) and with other observational products and reanalysis (Figure 6b). We find a strong correlation (R = 0.71,>99% significance level) between the salinity PC1 and the CalCOFI oxygen time series (Figure 6a). When comparing the PC1 from ORA-S3 to the SODA and ORA-S4 reanalysis, we find overall good agreement with correlations R=0.8 and R=0.75. The Argo data is also in agreement with the ORA-S3 but the timespan of the data is too short for any meaningful correlations. The ORA-S4 shows an anomalous higher salinity between 2000-2010 that is not evident in all the other datasets, including Argo and the CalCOFI oxygen data.

The alignment between the ORA-S3 salinity proxy (salinity PC1) and the observational oxygen data supports our hypothesis that the multi-decadal variability of the oxygen content is primarily controlled by ocean subsurface circulation dynamics, rather than biological and chemical processes. Additional support for this hypothesis is evident from the strong correlation (R = 0.71,>99% significance level) that exists between the CalCOFI oxygen time series and the saturation (solubility) of oxygen inferred from ECMWF ORA-S3 subsurface temperature and salinity fields (following equation 8 from *Garcia and Gordon* [1992]), which is expected since temperature and salinity are compensated on a given isopycnal surface [*Veronis*, 1972]. To further explore the consistency of the ORA-S3 reanalysis in capturing subsurface signals, we compare a time series of subsurface salinity anomalies from the ORA-S3 dataset with available long-term salinity and oxygen

observations (data courtesy of W. Crawford) at Ocean Station P (OSP) (Figure 7), located in the sub-polar gyre [50°N 145°W]. Although OSP is outside the CCS domain, the high and significant correlation between OSP observations and ORA-S3 (R=0.63 for salinity and R=0.38 for oxygen) confirms that the ORA-S3 accurately captures the large-scale dynamics of subsurface salinity and oxygen in Northeast Pacific region. This enables us to use salinity anomalies on the isopycnal 26.5 as a proxy for exploring the multi-decadal dynamics of subsurface oxygen variability along the Pacific eastern boundary upwelling system.
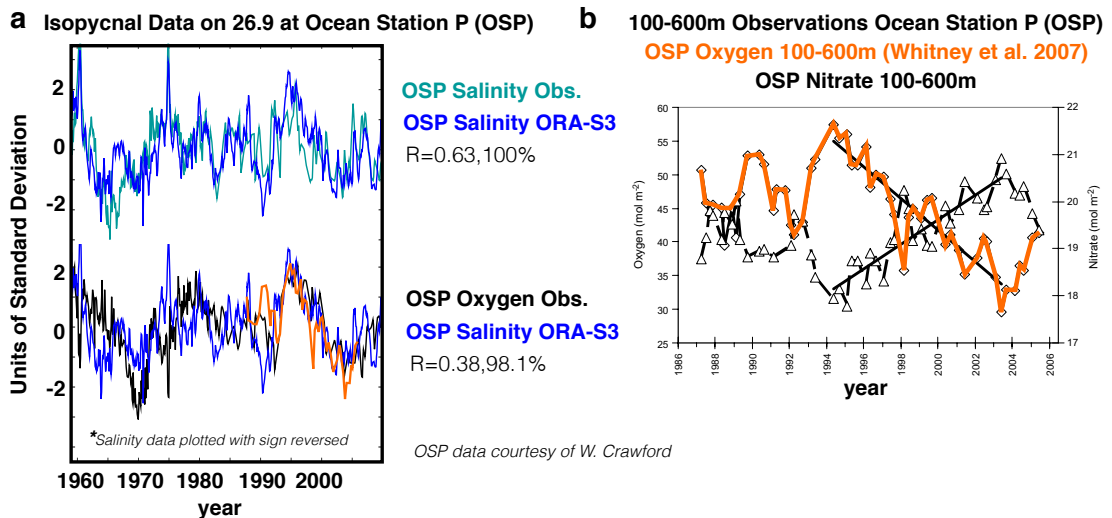
Figure 7. Subsurface salinity and oxygen at Ocean Station P (OSP). a. Time series of the salinity anomalies on the $\sigma_\theta = 26.9$ kg m^{-3} isopycnal surface from observations (light blue line) and from ECMWF ORA-S3 dataset (blue line) at OSP. Time series of the oxygen anomalies on the $\sigma_\theta = 26.9$ kg m^{-3} isopycnal surface from observations (black line) and integrated between 100-600 m (orange line, data from *Whitney et al*., [2007]). b. Figure 5 from *Whitney et al*., [2007]. Time series of nitrate (black line) and oxygen (orange line) integrated between 100 and 600 m at OSP.

3.4   Decadal dynamics of subsurface tracers and oxygen

We hypothesize that multi-decadal changes in subsurface tracers (e.g., salinity and temperature) and oxygen (e.g., $\sigma_\theta = 26.5\ kg\ m^{-3}$) in the CCS are controlled by anomalies that propagate along the path of the mean gyre circulation. To test this hypothesis, we explore the subsurface propagation dynamics of salinity anomalies, which we have identified as a close proxy for decadal changes of oxygen. We define an index of normalized salinity anomalies on $\sigma_\theta = 26.5\ kg\ m^{-3}$ along the coasts of Washington, Oregon, and California, that is the region of the CCS upwelling source waters and where the North Pacific Current reaches the eastern coastal boundary (Figure 8e, red box shows the region used to average the salinity; Figure 8h, red line shows the coastal salinity index). We then compute lead/lag correlation maps between this coastal salinity index and the salinity on the entire isopycnal surface over the eastern and central North Pacific (Figure 8a-f). At zero lag (Figure 8e), the correlation pattern shows a broad region extending from the coast to the offshore for about 1000km. This pattern decays at the coast at a 3-year lag (Figure 8f). In the growth phase at 3-year lead (Figure 8d), the correlation pattern shows that the center of action has shifted offshore along the axis of the southward branch of the sub-tropical gyre. The 3-year lead pattern is almost identical to the EOF1/PC1 of salinity in the CCS region (compare Figure 8d with Figure 6d), which we use as our proxy for the observed multi-decadal variability of oxygen in the CCS. We verify that by comparing PC1 to the coastal salinity index with a lead of 3-year, which show significant correlation (R= 0.77, Figure 8h). Further inspection of the spatial and temporal progression of the correlation maps at leads 6, 9 and 12 years (Figure 8a-c) shows a clear backward propagation of the salinity anomalies along the path of the mean gyre suggesting that multi-

decadal variability of salinity and oxygen in the CCS region is controlled by advection of anomalies along the mean circulation. In fact, at lead 12 years (Figure 8a) we find significant correlations along the axis of the North Pacific Current in excess of 0.65. These lead times are consistent with the mean advection timescales in the eastern North Pacific estimated using the ORA-S3 reanalysis dataset (Figure 10). To further visualize the connection between the gyre anomalies, salinity PC1 (i.e., proxy for oxygen) and the coastal salinity, we compare an index of gyre salinity anomalies (i.e., the average salinity anomaly in the green box of Figure 8a) with the salinity PC1 (Figure 8g) and the coastal salinity index (Figure 8i) with the appropriate lags of 9 and 12 years later. The time series exhibit strong and significant correlation R=0.59 (gyre salinity vs. PC1) and R=0.66 (gyre salinity vs. coastal salinity) with a dominant multi-decadal signal. These propagation dynamics are consistent with other reanalysis products (e.g., ORA-S4 and SODA, Figure 4). While ORA-S4 replicates the propagation pattern of the salinity anomalies found in ORA-S3 (compare Figure 8a-e to Figure 9a), with a slight expansion of the correlation signal at lead 12 years, SODA shows a general weakening and loss of significance of the propagation pattern (compare Figure 8a-e to Figure 9b). These differences may arise from the differences in the models and assimilations methods used to generate the reanalysis products [*Balmaseda et al.*, 2008; 2013; *Carton and Giese*, 2008]. For example, the assimilation scheme used in SODA does not preserve the integrity of subsurface water masses on isopycnals.

These results suggest that multi-decadal changes of salinity and oxygen in the CCS originate from subsurface anomalies in the North Pacific gyre rather than from the

California Undercurrent. Given the decadal timescale involved in the propagation of these

anomalies from the gyre, the decadal dynamics of oxygen may have inherent predictability.

Figure 8. Subsurface propagation of salinity anomalies. a, Lead/lag correlation maps between the salinity anomalies on the $\sigma_\theta = 26.5$ kg m^{-3} isopycnal surface and the

coastal salinity index from lead 12 years (panel a) to lag 3 years (panel f), in increments of 3 years. Only positive correlations are plotted in the shading. Contours represent the mean Bernoulli's stream function along isopycnal 26.5 showing the path of the mean subsurface circulation. The coastal salinity index (red line in panel h and i) is the average salinity anomaly on the $\sigma_\theta = 26.5$ kg m^{-3} isopycnal in the region of the red box (coordinates 126°W – 119°W and 32.5^{o}N – 48°N). The salinity PC1 (blue line in panel g and h) is the time series of leading mode of the salinity defined in the blue box (panel d). The salinity gyre index (green line, panel g and i) is defined as the spatially average salinity anomaly upstream the gyre in the region of the green box (coordinates 161°W – 137°W and 46°N – 50°N). The salinity gyre index leads the salinity PC1 and the coastal salinity index by 9 (panel g) and 12 years (panel i), respectively. The salinity PC1 leads the coastal index by 3 years (panel h). All the figures have been done using the ECMWF ORA-S3 dataset.

Figure 9. Lead correlation maps between the salinity anomalies on the $\sigma_\theta = 26.5$ isopycnal surface and the coastal salinity index from lead 12 to 0 years in increments of 3 years from a. ORA-S4 and b. SODA reanalysis products. Only positive correlations are plotted in the shading. Contours represent the mean Bernoulli's stream function along isopycnal 26.5 showing the path of the mean subsurface circulation.
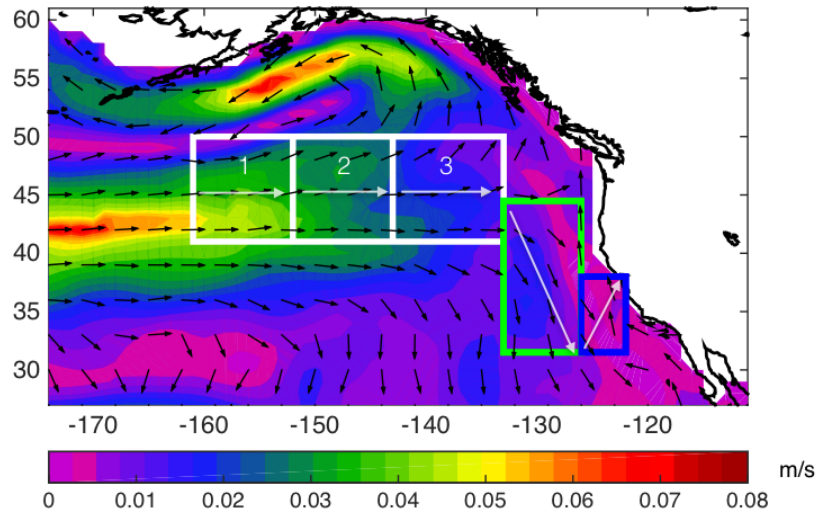
Figure 10. Mean speed of the currents on the $\sigma_\theta = 26.5$ kg m^{-3} isopycnal surface from ECMWF ORA-S3 dataset (color shading). The five boxes mark the mean extension of the significant anomalies (Figure 8a-e, patching region), the gray arrows represent the approximated path of the anomalies, and the black arrows represent the direction of the currents on isopycnal 26.5. Distance is calculated from the origin to the end of each arrow. In the region of the white box, the anomalies travel a total of 2196.6 km along the horizontal path in 2.66 years with mean speeds of 0.0368, 0.0303, and 0.0183 m/s for boxes 1, 2, and 3, respectively. In the green box, the anomalies travel with a mean speed of 0.0126 m/s along the distance covered by the arrows (~1567 km) in ~3.95 years. In the blue box, the anomalies travel with a mean speed of 0.0047 m/s along the distance covered by the arrow (~808.5 km) in ~5.46 years. The total amount of years that anomalies travel from the gyre to the coast following the arrows path is approximately 12 years, which is consistent with the propagation timescales in Figure 8 and 9.

3.5   Discussion and implications for decadal predictability of oxygen

The potential for long-term predictability of temperature, salinity, and nutrients associated with the propagation of subsurface anomalies along the North Pacific gyre has been identified in previous observational and modeling studies [*Chikamoto et al.*, 2015; *Rykaczewski and Dunne*, 2010; *Sasaki et al.*, 2010; *Taguchi and Schneider*, 2014]. Here we show that salinity anomalies, and its subsurface propagation dynamics from the North

Pacific gyre into the CCS region, lead to a skillful reconstructions of the observed multi-decadal changes in CCS oxygen (Figure 8). The significant correlation (R=0.66) between multi-decadal fluctuations of CCS coastal salinity (i.e., a close proxy of oxygen) and salinity in the North Pacific Gyre 12-year prior (Figure 8i) is suggestive of a strong relation, and predicts a new decade of low oxygen anomalies of the source waters that feed the CCS upwelling by 2020 (green time series in Figure 8i).

Although our results emphasize the role of the gyre-scale circulation in driving multi-decadal subsurface tracers anomalies in the CCS, previous studies have identified the CU as an important source of water mass anomalies in the CCS, especially in the coastal region within 100km from the coast and in the Southern California Bight (SBC) [*Bograd et al.*, 2008; *Bograd et al.*, 2015; *Gay and Chereskin*, 2009; *Lynn and Simpson*, 1987; *Meinvielle and Johnson*, 2013; *Nam et al.*, 2015; *Thomson and Krassovski*, 2010]. Although our results do not exhibit a clear propagation signal from the equator, some correlation signals are displayed in the southern part of the CCS domain, near the SBC (Figure 8 and 11), which may be associated with the CU dynamics. Furthermore, our analyses have focused on the large-scale CCS (see EOF1/PC1 Figure 6) rather than the narrow coastal boundary where CU dynamics are important. Future studies with high-resolution ocean models will be able to diagnose the interactions dynamics between the gyre-scale and CU signals, and their relative control on the anomalies of upwelled water masses.

Taken together, these results imply that monitoring the anomalies along the axis of the North Pacific Current may lead to decadal predictability of subsurface oxygen in the CCS and potentially of the low-frequency statistics of hypoxia along the California coast. However, the potential for decadal forecasts of oxygen in the CCS requires further testing

to assess its statistical robustness. This will require the use of an ensemble approach of retrospective ocean simulations for the period 1950-present with a high resolution model that adequately captures the regional circulation dynamics and scale interactions between the North Pacific gyre and the eastern boundary current system (e.g., structure and speed of the mean currents, vertical structure of temperature and salinity).

Although coarse resolution climate model ensembles are not adequate for testing the regional predictability of oxygen in the CCS, they do provide insight on the large-scale gyre dynamics. A recent analysis of the Community Earth System Model Large Ensemble (CESM-LE) [*Kay et al.*, 2015] project from 1920-2100 under the greenhouse forcing scenario RCP8.5 shows a significant declining trend of subsurface oxygen on isopycnal 26.5 originating in the western North Pacific and spreading along the North Pacific Current [*Long et al.*, 2016]. This declining trend is consistent among other climate model simulations and is likely related to a reduction in oxygen solubility from ocean warming and weak ventilation from stratification and circulation changes [*Doney et al.*, 2012; *Henson et al.*, 2017; *Keeling et al.*, 2010; *Long et al.*, 2016]. According to the CESM-LE [*Long et al.*, 2016] a strong declining oxygen trend will become evident in the eastern side of the North Pacific Current (e.g., at Ocean Station Papa, 50°N 145°W] in year ~2030, implying that CCS oxygen multi-decadal variability may be exceeded by climate change-induced deoxygenation trends within the next few decades.

The decadal and predictability dynamics of oxygen explored for the California Current System may be important in similar eastern boundary upwelling systems. However, when applying these results to different ocean tracers, for example pH (i.e., ocean acidification), it is important to consider that other dynamics associated with trend components (e.g.,

anthropogenic atmospheric CO_2) [*Bopp et al.*, 2013; *Hauri et al.*, 2009; *Hauri et al.*, 2013]

and different memory timescales (e.g., decay) may lead to a reduction of the variance

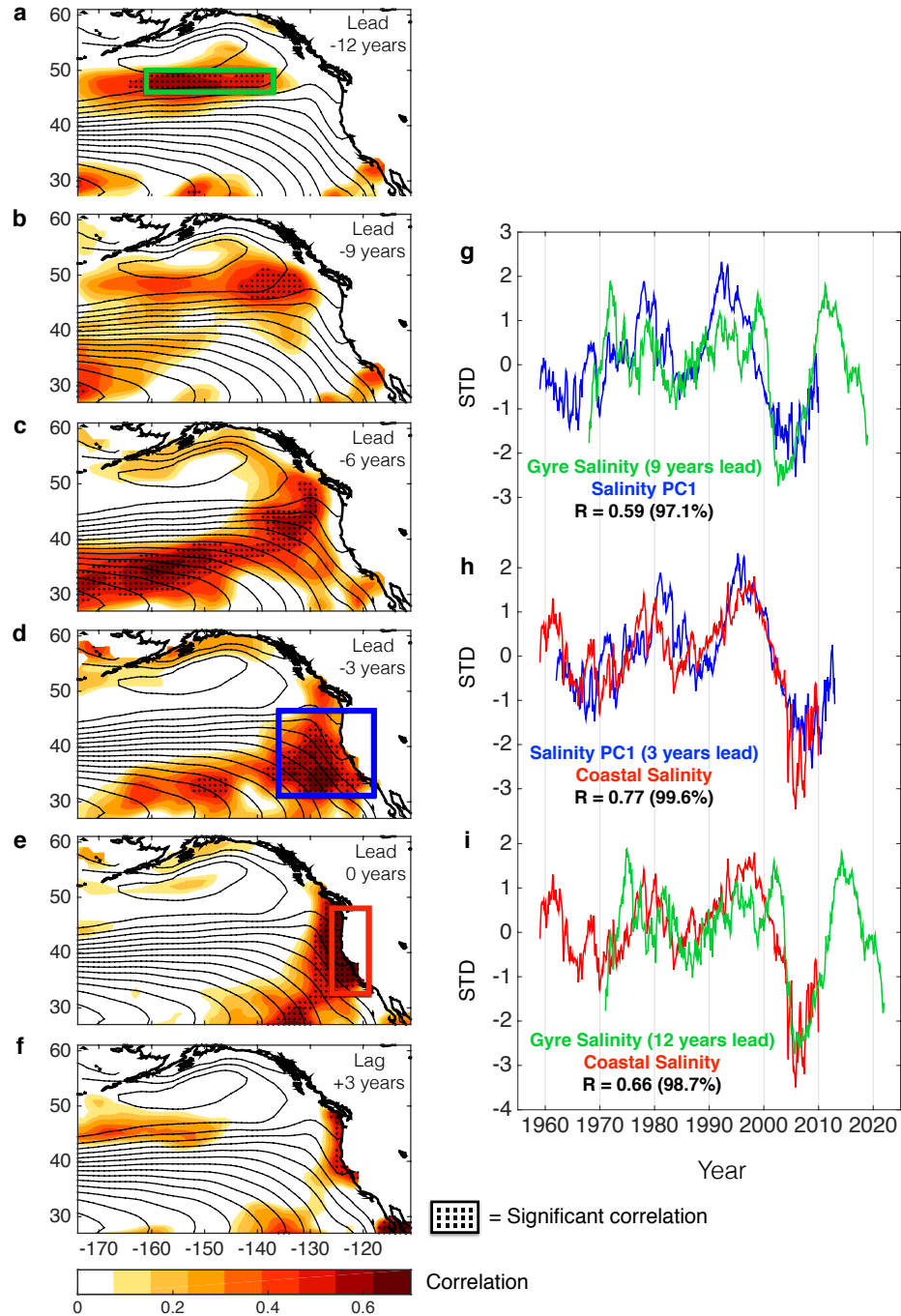explained by the decadal propagation of anomalies from the gyre-scale circulation.
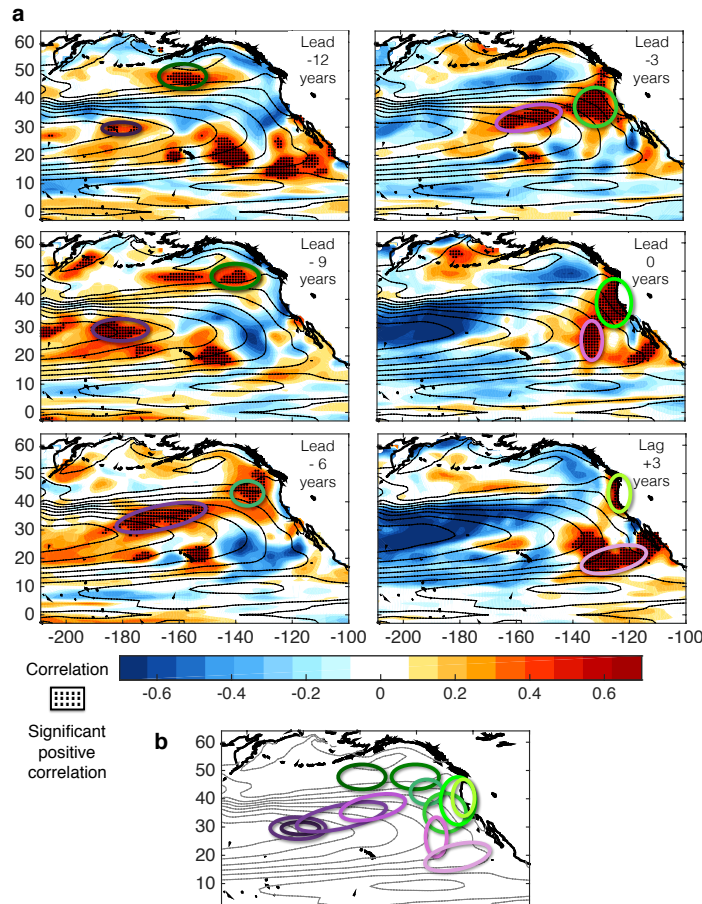
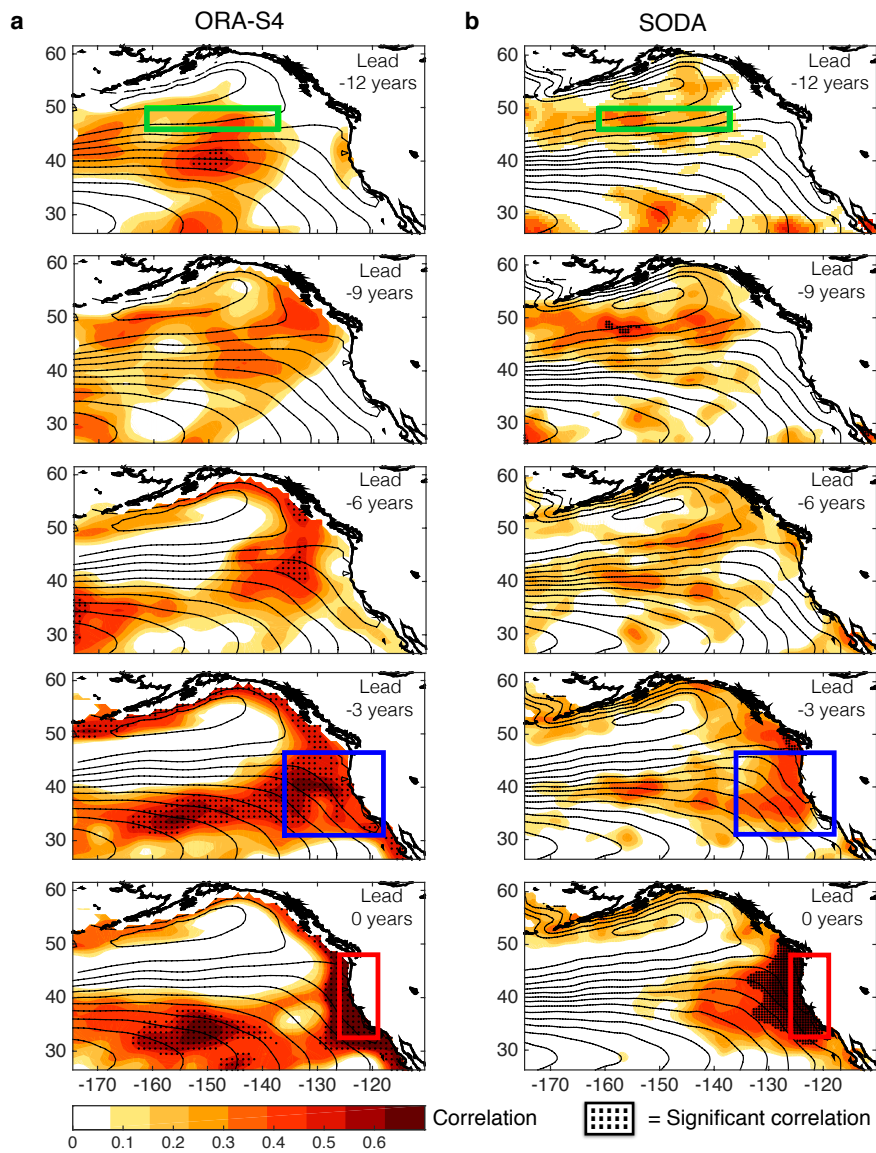**Figure 11. Subsurface propagation of salinity anomalies. a. Lead/lag correlation maps between the salinity anomalies on the $\sigma_0 = 26.5$ kg m^{-3} isopycnal surface and the coastal salinity index from lead 12 to lag 3 years in increments of 3 years. This figure is the same as Figure 3(a-f) but with an expanded domain and showing both the positive and the negative correlations). The green and purple ovals follow the propagation of the main positive anomalies. b. Summary of the propagation of the main positive anomalies. Contours represent the mean Bernoulli's stream function along isopycnal 26.5 showing the path of the mean subsurface circulation.**

CHAPTER 4.   DETERMINISTIC DYNAMICS OF NORTH PACIFIC OCEAN SUBSURFACE ANOMALIES

This work is under preparation to submit to the Journal of Climate.

4.1   Introduction

Previous results using basin-scale reanalysis products suggest that downstream advection of subsurface water-mass anomalies along the North Pacific Current (NPC) can be exploited for predicting decadal-scale changes of temperature, salinity, nutrients, and oxygen in key upwelling systems of the North Pacific, namely the Gulf of Alaska and the California Current System. However, it is unclear how far upstream along the gyre one can track these subsurface water-mass anomalies for reliable decadal predictions.

Building upon the results on Chapters 2 and 3, the main objectives of this chapter are to further (1) investigate the robustness of propagation of the subsurface water-mass anomalies, and (2) quantify the predictability (i.e., deterministic vs. intrinsic variability) associated with the propagation of the subsurface water-mass anomalies from upstream of the gyre into the CCS upwelling system. Our approach to this investigation is to use an ensemble of eddy-resolving hindcasts of the Regional Oceanic Modeling System (ROMS) from 1959-2009 over the North Pacific. The results from the ensemble will help us to better understand the physical processes behind the generation and propagation of the subsurface water-mass anomalies and also to diagnose the forcing dynamics that drive the deterministic (i.e., forced) and predictable low-frequency variability.

This chapter is organized as follows: Section 4.2 provides a brief description of the model and outlines the ensemble approach. Section 4.3 validates the mean structure and state of the subsurface circulation in the model. Section 4.4 explores the deterministic versus the intrinsic variance in the model. Section 4.5 compares the robustness of the eastward propagation of the subsurface anomalies previously presented, and Section 4.6 quantifies the potential decadal predictability associated with propagation of the subsurface anomalies.

4.2   Model setup and domain

To conduct the Pacific ensemble, we use the Regional Ocean Modeling System (ROMS). ROMS is a three-dimensional, free-surface, eddy-resolving primitive equation ocean model that takes into account the hydrostatic and Boussinesq assumptions to solve the Reynolds-averaged Navier-Stokes equations.   The hydrostatic primitive equations are solved using a split-explicit time-stepping algorithm that requires the separation of barotropic (fast) and baroclinic (slow) modes. ROMS uses generalized orthogonal curvilinear coordinates in the horizontal and stretched terrain-following coordinates (sigma-coordinates) in the vertical on an Arakawa C-grid [*Haidvogel et al.*, 2000; *Shchepetkin and McWilliams*, 2005; 2009]. The vertical mixing of tracers and momentum is determined by the K-profile parameterization (KPP) scheme [*Large et al.*, 1994]. ROMS has the option of different higher-order advection schemes, accurate horizontal pressure-gradient algorithms, vertical mixing schemes, several subgrid-scale parameterizations, algorithms for the application of external data at open boundaries, biological modules, and data assimilation.   Most technical details of ROMS are described in Shchepetkin and McWilliams [1998; 2003a; 2005], and in *Penven et al.* [2006].

ROMS has shown its potential as an ocean prediction model thanks to successful results obtained in various regions. In the Pacific Ocean, some examples of these studies are related to the dynamics of mesoscale processes in the California Current System (CCS) [*Di Lorenzo et al.*, 2005; *Moore et al.*, 2011a; 2011b], the Gulf of Alaska [*Combes and Di Lorenzo*, 2007; *Hermann et al.*, 2009; *Hinckley et al.*, 2009], and the Peru-Chile System [*Cambon et al.*, 2013; *Penven et al.*, 2005]; low-frequency variability of main climate variables and nutrients [*Di Lorenzo et al.*, 2008; *Chhak et al.*, 2009; *Jacox et al., 2014*], and large-scale circulation [*Curchitser et al.*, 2005]. These studies, among others, validate the model as a potential tool for studying interannual and interdecadal variability in the Pacific Ocean.

ROMS currently includes a variety of versions developed by different institutions; this study employs a version of ROMS developed at the University of California, Los Angeles (UCLA ROMS). Unlike other current versions (Rutgers and AGRIF ROMS), this version stands out because of three main features. One is related to the time-stepping algorithm. The algorithm for both momentum and tracer equations is the Leap-Frog with third-order Adams-Moulton predictor-corrector (LF–AM3 PC), which makes the code more efficient since the terms on the right-hand side of the equations are not stored from one-time step to another. Another feature in UCLA ROMS is the coupling between barotropic and baroclinic modes, which occurs during the corrector stage of the 3D momentum step. More details about these features are found in *Shchepetkin and McWilliams* [2005]. Finally, the main feature is the unprecedented speed at which UCLA ROMS performs eddy-resolving calculations for a basin as a result of the dimensional division of the main domain and the parallelization of the ROMS code via shared (open MP) and distributed memory (MPI).

4.2.1 ROMS configuration

In this study, the basin model domain covers the North Pacific Ocean and ranges from 12.4º to 65ºN and 105.4ºE to 83.9ºW. We use two different resolutions of the North Pacific, a coarser (i.e., non-eddy resolving) and finer (i.e., eddy-resolving) grids. The average horizontal resolution of the coarser and finer grid space is approximately 23 km and 12 km (Figure 12, panel b), with a total number of grid points of 592 x 256 and 1186 x 514, respectively. Both grids contains 40 vertically stretched generalized terrain-following coordinates with stretching parameters of $\theta_s = 7.5$, $\theta_b = 0.5$ and $h_c = 350$m (following the notation of *Song and Haidvogel* [1994]). This configuration of the vertical grid enhances the resolution towards the surface and the bottom. The bathymetry in the two models is also the same. The raw bathymetry of the models is interpolated from the two-minute elevation and bathymetric data (ETOPO2) and smoothed using a Laplacian operator. Further smoothing by iteratively applying a filter reduces the r-factor ($r = \Delta h/h$) below 0.16, or the ratio of the maximum difference between adjacent grid cell depths and the mean depth at that point. A computation with negligible pressure gradient errors requires a small r-factor.

4.2.2 Spin-up simulations

A schematic diagram of the spin-up and hindcast (historical) model simulations are shown in Figure 12a. The upper ocean equilibrates on much shorter time scales than the subsurface and deep ocean. To ensure the subsurface ocean reaches the state of statistical equilibrium, we start the spin-up integration using a coarser North Pacific grid with an average resolution of 23 km (Figure 12b). In our spin-up simulation, the surface properties reach

equilibrium after approximately 25 years of integration, while subsurface properties need at least 300 years. The 23km model (ROMS23) is integrated with historical forcing from 1959 to 2009, starting from year 0, for 1224 years, or 24 of the 51-year cycles. The spin-up is completed by interpolating the last January (i.e., January of year 1225) properties to the 12 km model (ROMS12) grid and integrating for 153 more years (i.e., three 51-year cycles) to allow for equilibrium adjustment of the subsurface properties. Therefore, the total years of spin-up integration is 1337 years.
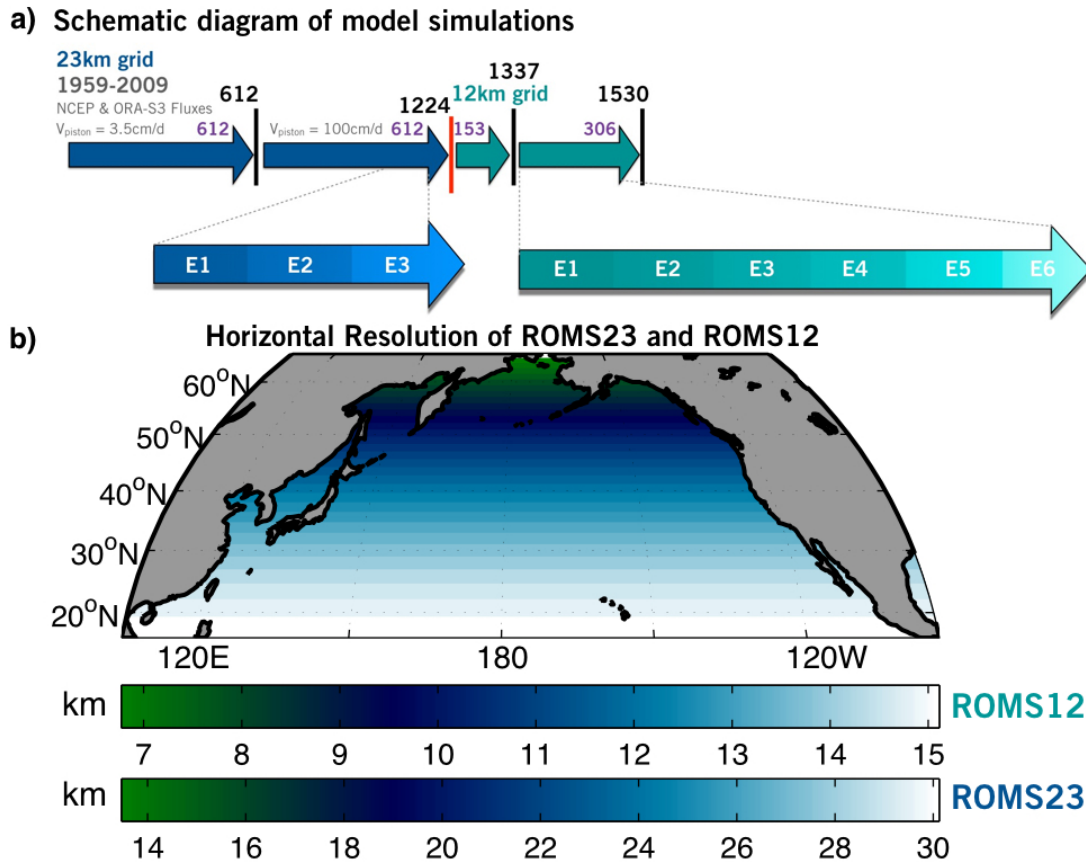
Figure 12. (a) Schematic diagram of the model simulations. The red line marks the end of using the grid ROMS23. Year 1337 corresponds with the end of the spin-up simulations. (b) Horizontal resolution (km) of the model for the 23 and 12 km grids, ROMS23 and ROMS12, respectively.

As surface forcing conditions, we use mean-seasonal climatological heat and freshwater flux and mean-seasonal time-dependent (1959-2009) wind-stress flux. We use climatological monthly freshwater and short radiation fluxes derived from the National Center for Environmental Prediction/National Center for Atmospheric Research (NCEP/NCAR) [*Kalnay et al.*, 1996] reanalysis at a 2.5º resolution. We also use climatological surface heat fluxes and detrended time-dependent (1959-2009) wind-stress fluxes derived from the European Centre for Medium-range Weather Forecasting (ECMWF) Ocean Reanalysis System (ORA-S3) at a 1º resolution. To avoid long-term drifts in the SSTs associated with errors in the heat surface fluxes, the model includes a correction term dQdSST (i.e., net heat flux sensitivity to SST) that varies spatially and seasonally and nudges the monthly SST of the model to climatological monthly ECMWF ORA-S3 SST averaged from 1959 to 2009. This dQdSST is extracted from the Comprehensive Ocean-Atmosphere Data set (COADS), more information about this term is described in *Barnier et al.* [1995].

In addition, a salinity restoring term is applied at the ocean surface, which works in a similar approach as the dQdSST term. Although the salinity restoring is unphysical, its use in ocean general circulation models (OGCM) maintains a more realistic SSS [*Griffies et al.*, 2009]. This standard restoring is designed to prevent the drift of the basin mean SSS, while allowing the drift of the basin salinity. This restoring is applied also to try to compensate for the lack of freshwater input in the Gulf of Alaska and Bering Sea via SSS. During the first 612 years of the spin-up, a weak salinity restoring (V_{piston} of 3.5 cm/d or 50 m/4y) was applied (following *Yin et al.,* 2009), however, by the end of those 612 years, the subsurface water-masses were not well represented. To ensure a better representation

of the model water mass structure, we increase the V_{piston} to a value of 100 cm/d, and we run the rest of the simulations (i.e., from year 613) with this new strong salinity restoring. An explanation of how to obtain this value of V_{piston} or strong salinity restoring can be found in Appendix A.

The model has an open boundary to the south of the domain, where the boundary fields are nudged to detrended monthly fields derived from the ECMWF ORA-S3 data set from 1959 to 2009 in all the integrations. Again, the monthly boundary forcing is repeated every 51 years. We initialized the ocean at year 0 using mean climatological January ECMWF ORA-S3 variables and applying a weak salinity restoring (~3.5 cm/d). At year 612, when we applied the strong salinity restoring, the 23 km model is initialized with the last January computed (i.e., January of year 613), and run for the other 612 years (a total of 1224 years). Finally, we initialized the 12 km model by interpolating the state of the ocean of the last January (i.e., January of year 1225) of the 23 km model, which requires a second spin-up of 153 years.

4.2.3   Hindcast simulations and Ensemble approach

Once the subsurface ocean reaches statistical equilibrium with the 12 km grid after a few centuries (~153 years, 1337 years in total), we start the first ensemble member using the last January of the 154 year run with the 12km grid. In the ensemble integrations, the model is forced with the same surface and boundary forcing conditions used for the time-dependent spin-up simulation described in section 4.2.2. During the hindcast simulations nudging to time-dependent SST and SSS remain the same, which ensures a correct formation of water mass in the subsurface.

In the ensemble approach, the only difference among the ensemble members is that the initial condition changes from one member to the next. Because we use a cyclic forcing (same 51 years forcing from 1959-2009), every last January simulated in one ensemble member acts as an initial condition for the following ensemble member. The selection of the initial condition is not as critical as it is in weather forecasting because the ensemble members will be integrated from 1959 to the 2009. Over such long periods of integration small errors will grow and reach saturation. This period, when large amounts of instrumental data is available for model/observation inter-comparisons, represents the time span of the model hindcast.

Due to the long computational time required, only three member of the ensemble have been integrated to date. Because we want to take advantage of the long integration of the model, we will compare the results from ROMS12 ensemble with an ensemble of three members from the ROMS23 model. These three members correspond to the last 153 years (51 years each) before the interpolation from the coarser to the finer grid (before the red line in Figure 12a). We will use this additional archive to compare the low-frequency variability of the subsurface water-mass properties of the eddy-resolved and non-eddy-resolved circulation in the ROMS model.

To achieve the first goal of this chapter, we apply an ensemble approach to separate the deterministic low-frequency variance (i.e., ensemble mean) from the ocean's internally-driven variance (i.e., ensemble spread). We use six ensemble members from the ROMS model (i.e., a single-model ensemble approach). Although a larger number of members for the ensemble would be desirable, six members represents a compromise between the constraints of computing and results from other studies with ROMS. It is usually

computationally expensive for large ensembles to be produced when the number of model grid points is large, so some studies have used fewer than six members. For example, *Davis and Di Lorenzo* [2014b] used a three-member ROMS ensemble to separate the intrinsic and deterministic fractions of eddy variability in the CCS region.

4.3 Validation of the surface model against reanalysis products

The main focus of the validation is on the decadal variability of the surface properties in order to verify the performance of the surface nudging approach for surface temperature and salinity in the model. The decadal climate variability of the North Pacific Ocean is described by two dominant statistical modes: the Pacific Decadal Oscillation (PDO; Mantua et al., 1997) and the North Pacific Gyre Oscillation (NPGO; Di Lorenzo et al., 2008). By performing an empirical orthogonal function (EOF) analysis of the output from the model hindcasts with the coarser and finer resolution grids, we are able to isolate the PDO and the NPGO modes of variability. We define the model PDO and the NPGO indexes as the first and second principal components (i.e., PC1 as PDO and PC2 as NPGO) of the ensemble mean SSTa. As seen in Figure 13ab, the model is able to capture the spatial characteristic of the PDO and NPGO. Although we only show results from the spatial modes using the ROMS12 ensemble, similar spatial patterns are reproduced with ROMS23. The model also tracks closely the temporal evolution of observed PDO and NPGO indexes Figure 13c.
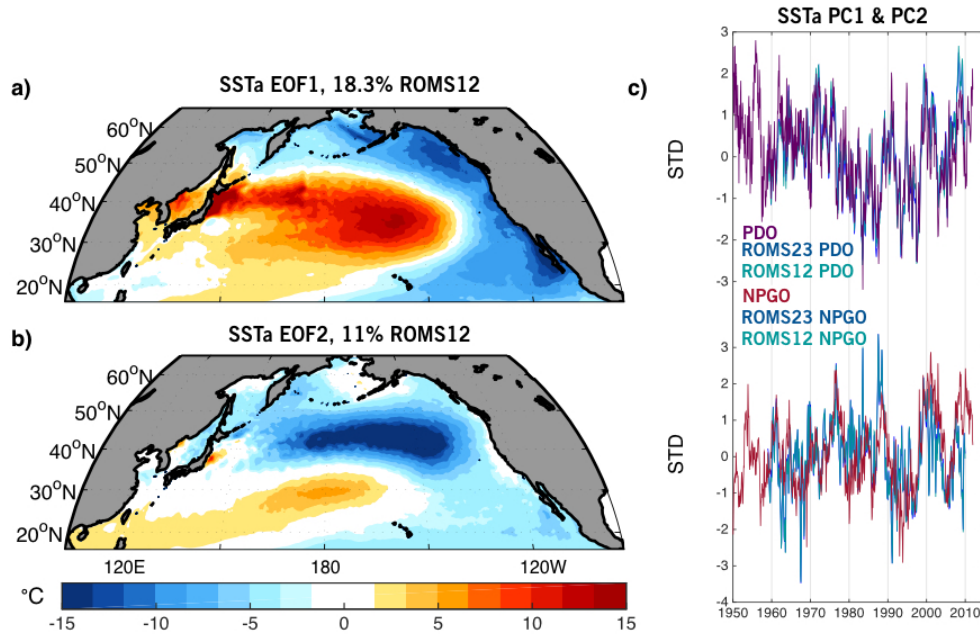
Figure 13. Spatial pattern of the first (a) and second (b) mode of SST variability in ROMS12. Same patterns are found in ROMS23 (c) (top) Time series of the observed PDO index (purple line), and mean ensemble PC1 of SSTa from ROMS23 and ROMS12 (blue and aqua line respectively). (bottom) Time series of the observed NPGO index (dark red line), and mean ensemble PC2 of SSTa from ROMS23 and ROMS12 (blue and aqua line respectively). Mean correlation between the observed and the modeled PDO and NPGO is 0.88 (>99%) and 0.56 (>99%), respectively. All time series are plotted in standard deviation units.

To ensure a good representation of subsurface properties, and compensate for the lack of freshwater inputs, we applied a strong SSS relaxation in our simulations. Figure 14 panels a and b show the annual mean ensemble SSS and its differences with respect to the mean SSS from ORA-S3. Although the model reproduces the SSS reasonably well, quantitative differences still exist. Annual mean SSS biases in ROMS12 are within ± 0.2 psu throughout most of the North Pacific Ocean. The exceptions are the central subtropical gyre, which is less salty, by over 0.5 psu, and a small region in the western boundary current region, which is too salty, by over 0.6 psu (Figure 14b). Despite these biases in the representation of the mean state of the SSS, the model closely tracks the decadal variability of the SSS. We find

a mean correlation of 0.6 (>99%) between the ROMS12 SSS and ORA-S3 SSS in different selected regions, as seen in the Figure 14c. Similar results are found in ROMS23, (not shown).
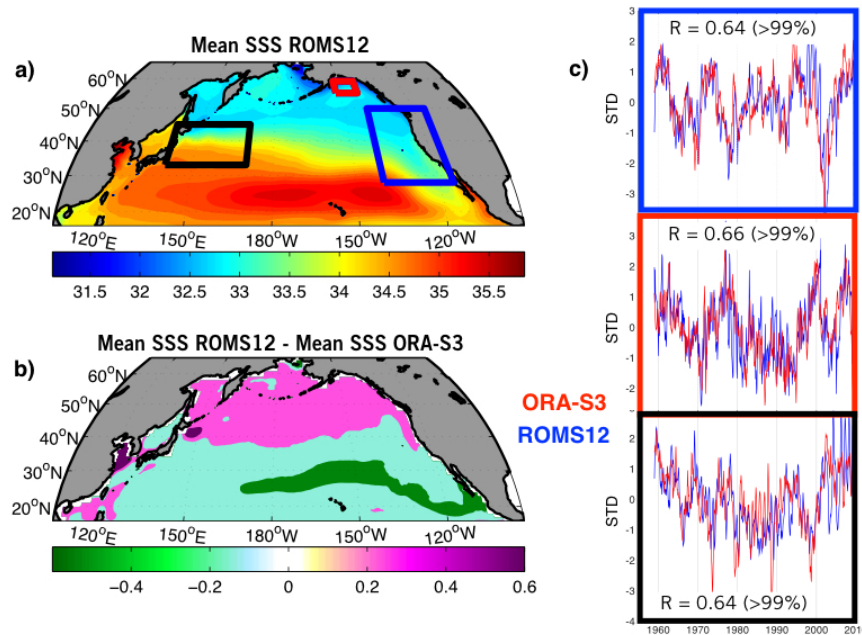
Figure 14. (a) Ensemble mean SSS from ROMS12. (b) Difference between the ensemble mean SSS form ROMS12 and the mean SSS from ORA-S3. (c) Time series of averaged SSSa from ROMS12 (blue lines) and ORA-S3 (red lines) in different regions of the North Pacific. These regions are depicted in (a).

We complete the validation exercise by comparing the subsurface mean state of the model to reanalysis data. Vertical cross sections of the mean ensemble annual salinity (Figure 15) show an overall slightly saltier subsurface ocean in the ROMS compared to the mean state in ORA-S3. In ORA-S3, the low-salinity water that emanates from high latitudes at 400-600 m tracks the North Pacific Intermediate Water (NPIW). In ROMS12, this main salinity minimum in the subtropical North Pacific is saltier than in ORA-S3. However, the depth and its potential density are well-defined, 300-700 m and 26.7 26.9 kg m^{-3}, around 30°-

45°N [*Talley*, 1993]. In the thermocline, the model does a much better job of capturing the reanalysis north–equator structure of the salinity, although it is still slightly fresh at higher latitudes. It is important to keep in mind that there is restoration to reanalysis surface salinity in the model that forces modeled surface salinity to be close to reanalysis.
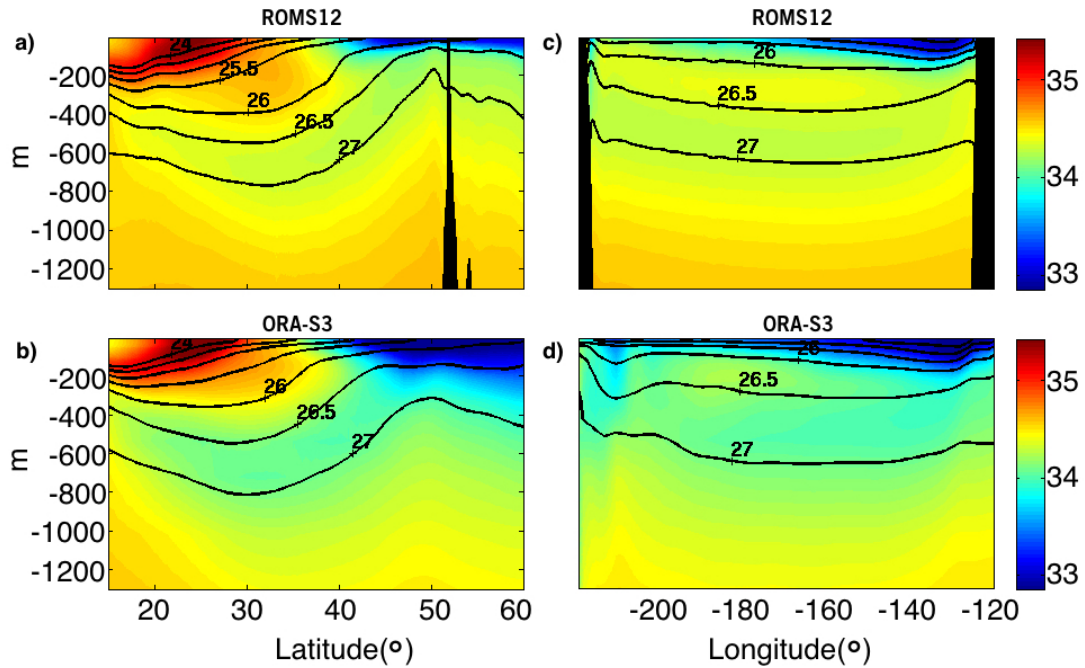
Figure 15. Meridional sections, latitude versus depth (m), of annual mean salinity (shading) and potential density (contours) along 180° from (a) ROMS12 and (b) ORA-S3. Zonal sections, longitude versus depth (m), of annual mean salinity (shading) and potential density (contours) along 40°N from (c) ROMS12 and (d) ORA-S3.

Although the vertical structure of the modeled salinity is slightly saltier than in ORA-S3, the model is able to reproduce the spatial mean structure of the potential density in good agreement with the reanalysis. In the previous chapters, we focused our analysis in the water-mass properties along the isopycnal $\sigma_\theta = 26.5\ kg\ m^{-3}$ derived from the reanalysis products. Since the isopycnal 26.5 ventilates in the Gulf of Alaska during the winter months, in both models (ROMS12 and ROMS23), we focus our analysis on the isopycnal

$\sigma_\theta = 27 \ kg \ m^{-3}$. Specifically, we use water-mass properties along the isopycnal 26.9 and 27 from ROMS23 and ROMS12, respectively. The main reasons for choosing different isopycnal layers depending on the resolution of the models are: (1) their depth closely follows the depth of isopycnal 27 in the reanalysis data (Figure 16) and (2) neither of them ventilate during the winter months. Through the rest of the work we will refer to isopycnal 26.9 in ROMS23 as isopycnal 27 for simplicity when comparing with isopycnal 27 in ROMS12 and ORA-S3.
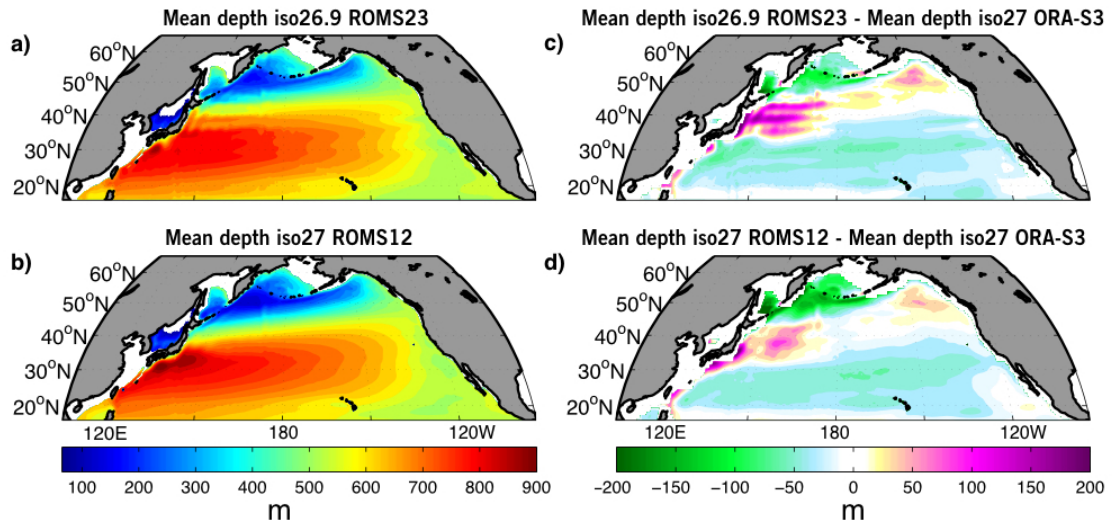
Figure 16. Mean ensemble depth of the isopycnal 26.9 from ROMS23 (a) and isopycnal 27 from ROMS12 (b). Depth difference between the isopycnal 26.9 from ROMS23 (c) and isopycnal 27 from ROMS12 (d) and isopycnal 27 from ORA-S3.

The mean depth of 27 isopycnal is characterized by a bowlshape in the subtropical gyre with depths of ~700 ± 50 m in the KOE and ~500 ± 50 m in the CCS region (Figure 16a, b). While in the western boundary, both models represent a deepening in the isopycnal 27 of about 100 m with respect the reanalysis (Figure 16c, d), in the subtropical gyre, the modeled isopycnal layer is shallower (~50-70m) than in the reanalysis. There is a good

agreement in the region along the path of the North Pacific Current (NPC), which is our region of interest since previous results show the propagation of the subsurface anomalies from the North Pacific gyre into the GOA [*Pozo Buil and Di Lorenzo*, 2015] and the CCS regions [*Pozo Buil and Di Lorenzo*, 2017].

4.4   Deterministic vs. intrinsic variability of subsurface water-mass properties

We perform a side-by-side comparison of results of the subsurface water-mass properties in the eddy-resolved (ROMS12), non-eddy-resolved (ROMS23), and reanalysis (ORA) ensembles. This last ensemble consists only of two members: ECMWF ORA-S3 [*Balmaseda et al.*, 2008] and ORA-S4 [*Balmaseda et al.*, 2013]. As in the previous chapter, we focus our analysis on the subsurface salinity variability as the main water-mass property. Comparisons of the model ensembles with the reanalysis data allow us to separate the deterministic and intrinsic fractions of the low-frequency subsurface salinity variability. First, we compute the correlation of the subsurface salinity anomalies from each ensemble member with the mean subsurface salinity anomalies from the ORA ensemble. The final correlation maps (Figure 17 panel a for ROMS23 and panel b for ROMS12), shows the ensemble average correlations between each model member and the reanalysis ensemble. The average correlation maps reveal a region of strong positive correlation located in the sub-polar gyre, centered around the bifurcation of the NPC. This region is wider and larger in ROMS23, extending until western boundary. In ROMS12, this positive correlation is confined in a narrower region along the path of the NPC and extends south into the CCS reaching most of the eastern boundary coast. Similar regions of high versus low correlation between the two ROMS models and ORA are found if we apply a low-pass filter of 5 years to the subsurface anomalies before computing the correlations (Figure 17

panel c for ROMS23 and panel d for ROMS13). After filtering out the high frequencies, the correlation in both models is increased and the region of maximum correlation is expanded.
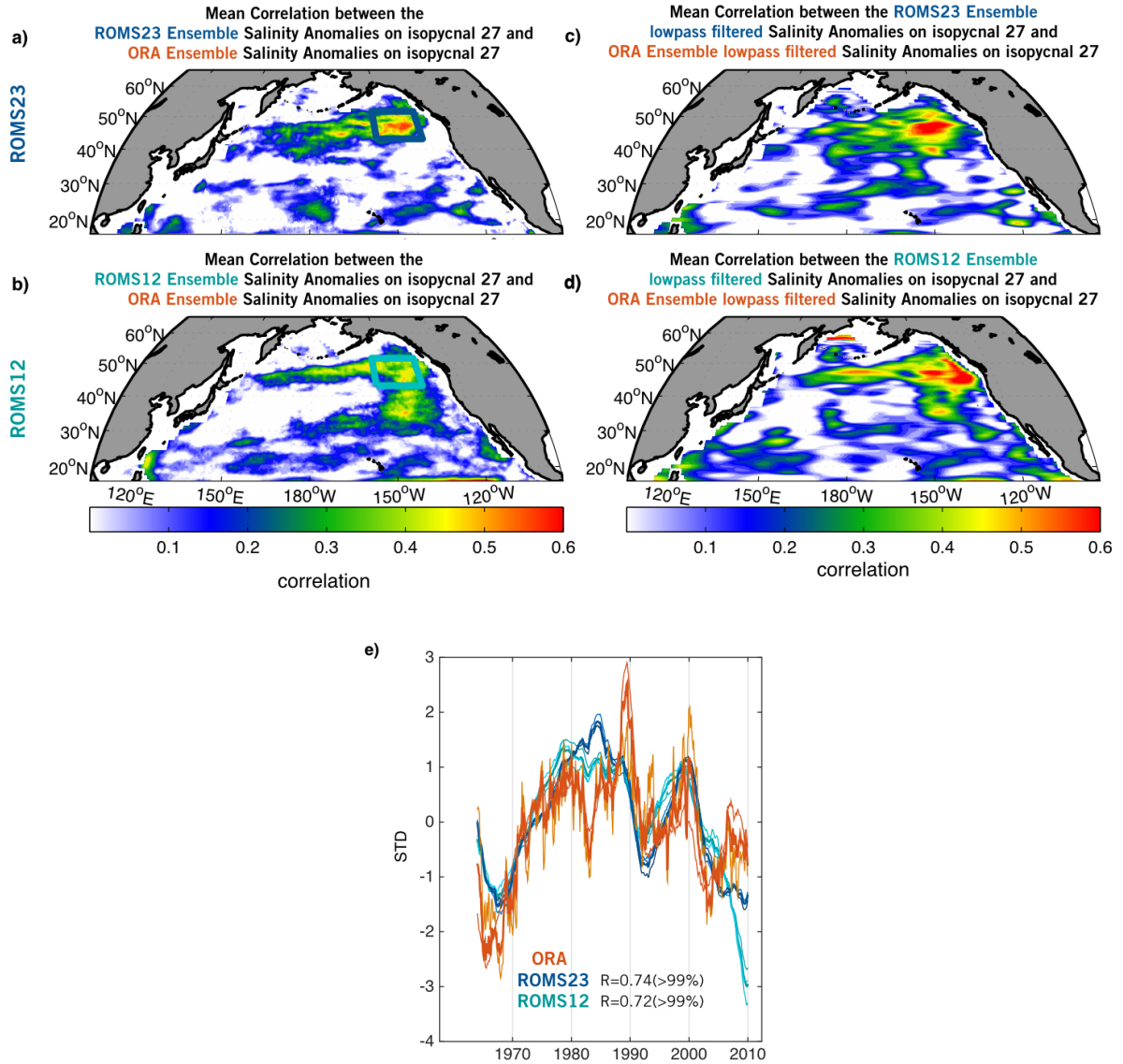
Figure 17. (a) Ensemble average correlation between the ensemble salinity anomalies on isopycnal 26.9 from ROMS23 and salinity anomalies on isopycnal 27 from the ORA ensemble. (b) Same as in (a) but for salinity anomalies on isopycnal 27 from ROMS12. (c) and (d) Same as in (a) y (b) for lowpass filtered salinity anomalies. (e) Time series of subsurface salinity anomalies averaged in the region of boxes (152.9°W – 135.4°W and 43.6°N – 52°N). Thinner lines represent each ensemble member and thicker lines the ensemble mean. Blue lines correspond to anomalies from ROMS23, aqua lines from ROMS12, and orange lines from ORA.

Then, we compute the average correlation among each ensemble members in the models (Figure 18, panel a for ROMS23 and panel b for ROMS16). These correlation maps are a representation of the ensemble spread in the models, where high correlation corresponds to less spread and more consistency among the ensemble members and low correlation corresponds to larger spread and less consistency among the ensemble members. In both models, we can observe less consistency among the members of the ensemble (i.e., larger spread) in the region of the subtropical gyre and in the KOE. In ROMS12 the spread is larger and extends all the way from the western to the eastern boundary of the subtropical gyre. There is significant agreement (i.e., less spread) between the ensemble members of both models in the region of the sub-polar gyre. This agreement is larger between the members of ROMS23 ensemble compared with ROMS12. Another main difference between the results from ROMS23 and ROMS12 is present in the coastal region of the CCS. While there is good consistency among the member of the ROMS23 ensemble, less consistency appears among the members of the ROMS12 ensemble extending to the southern CCS. The low-correlation regions found among the ensemble members are due to intrinsic variability and are even greater when comparing the eddy-resolving with the coarser ensemble model (ROMS12 vs ROMS23).

The same regions of high and low correlation (i.e., larger and smaller spread) are found when we apply a low pass filter of 5 years to the data before computing the correlations (Figure 18, panel c from ROMS23 and panel d from ROMS12). The regions with high consistency among the ensemble model are expanded to the west and south of the sub-polar gyre, and present higher correlations values in both models. The regions of larger

spread are confined again to the subtropical gyres and to narrower regions along the eastern and western boundaries of the domain.

Filtering out the high frequencies in both models reproduces the same regions of larger versus lesser spread in the models (Figure 18c, d). In addition, it increases the values of the correlation inside the same ensemble of the model, (e.g., ROMS12 vs filtered ROMS12), but these values of correlation are still lower compared to the coarser resolution ensemble (i.e., ROMS12 vs ROMS23).
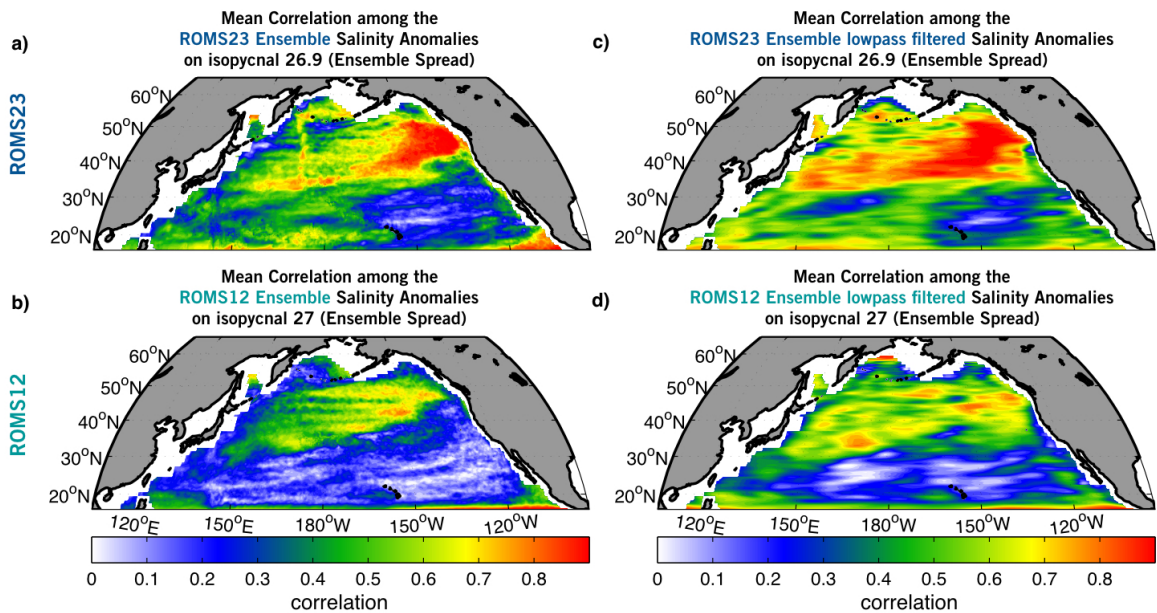
Figure 18. Mean correlation among the ensemble salinity anomalies on isopycnal 26.9 kg/m^3 from ROMS23 (a) and isopycnal 27 kg/m^3 from ROMS12 (b). (c) and (d) Same as in (a) and (b) but for lowpass filtered anomalies.

Taking together these results, we can isolate a main region of strong deterministic (i.e., potential predictability) variance in the core of the NPC and in the sub-polar gyre, and two regions of intrinsic (i.e., limited potential predictability) variance in the KOE and in the subtropical gyre. The regions of intrinsic and deterministic variance inferred from

comparing the model ensemble members, are also consistent with comparison against the ECMWF ocean reanalysis.

Figure 17e shows time series of area-mean subsurface salinity anomalies averaged in the region of deterministic variance where more correlation is found between both models and the reanalysis (NPC bifurcation region: 152.9°W – 135.4°W and 43.6°N – 52°N). Although the subsurface salinity in the reanalysis exhibits higher frequency variability than the models, both models are able to reproduce the multi-decadal low-frequency variability of the subsurface salinity of the reanalysis. (R=0.74, >99% from ROMS23 and R= 0.72,>99% from ROMS12). We also find a large consistency in the timings of maxima and minima of the anomalies between both models. Same results are found when we filter out the high frequencies (not shown).

4.5 Comparing ROMS propagation dynamics with reanalysis

To investigate the robustness of the propagation of the subsurface water-mass found previously [*Pozo and Di Lorenzo*, 2017], we compare results from the reanalysis data with the two ensembles of the ROMS model. Specifically, we examine the propagation dynamics of the subsurface salinity anomalies on isopycnal $\sigma_\theta = 27 \; kg \; m^{-3}$ in the CCS and determine how far upstream along the gyre we can track them. Although we found that in the CCS variability is not controlled by deterministic dynamics, it is still potentially predictable using the propagation circulation dynamics.

Following the same approach described in *Pozo Buil and Di Lorenzo* [2017], we define an index of normalized salinity anomalies on $\sigma_\theta = 27 \; kg \; m^{-3}$ in the CCS region defined by the coordinates 136°W – 118°W and 31°N – 46.5°N (Figure 22 panel a, red square), which

is the same region used for the PC1 and EOF1 (see blue square in Figure 6d). We then compute lead/lag correlation maps between this PC1 salinity index and the salinity on the entire isopycnal surface over the North Pacific (Figure 19 a, b and c for ORA-S3, ROM23 and ROMS12, respectively). These are the average correlation maps of each ensemble of ROMS23 and ROMS12, and for the reanalysis, we use ORA-S3. At zero lag, the correlation maps of the models and the reanalysis shows a strong correlation region that extends offshore. In ORA-S3 this higher correlation centers in two cores regions, one in the northern and one in the southern CCS. ROMS23 and ROMS12 show a similar pattern, but with higher correlation in the coarser model. This is caused by the larger spread of the ensemble found along the CCS coast in the ROMS12. The white regions along the eastern and western coasts in ROMS corresponds with the isopycnal outcrop masks. In the growth phase at 2-4 years lead the correlation maps shows the center along the axis of the southward branch of the subtropical gyre. The correlation in these centers is higher in the model cases than in ORA-S3. By 6-year lead the higher correlation is centered in the NPC bifurcation, the region of the stronger deterministic variance depicted in Figure 17a, b (blue squares). Further inspection of the spatial and temporal progression of the correlation maps at leads 8, 10 and 12 years shows a decay of the correlations center (as seen in previous results [*Pozo Buil and Di Lorenzo*, 2017] in ORA-S3. In contrast, ROMS23 and ROMS12 show a clear backward propagation of the salinity anomalies along the path of the mean gyre all the way to the western boundary. After 12 years lead, the correlation decays in both models. The same results are obtained by selecting a coastal index of the CCS (same as red box in Figure 8e, figure not shown).
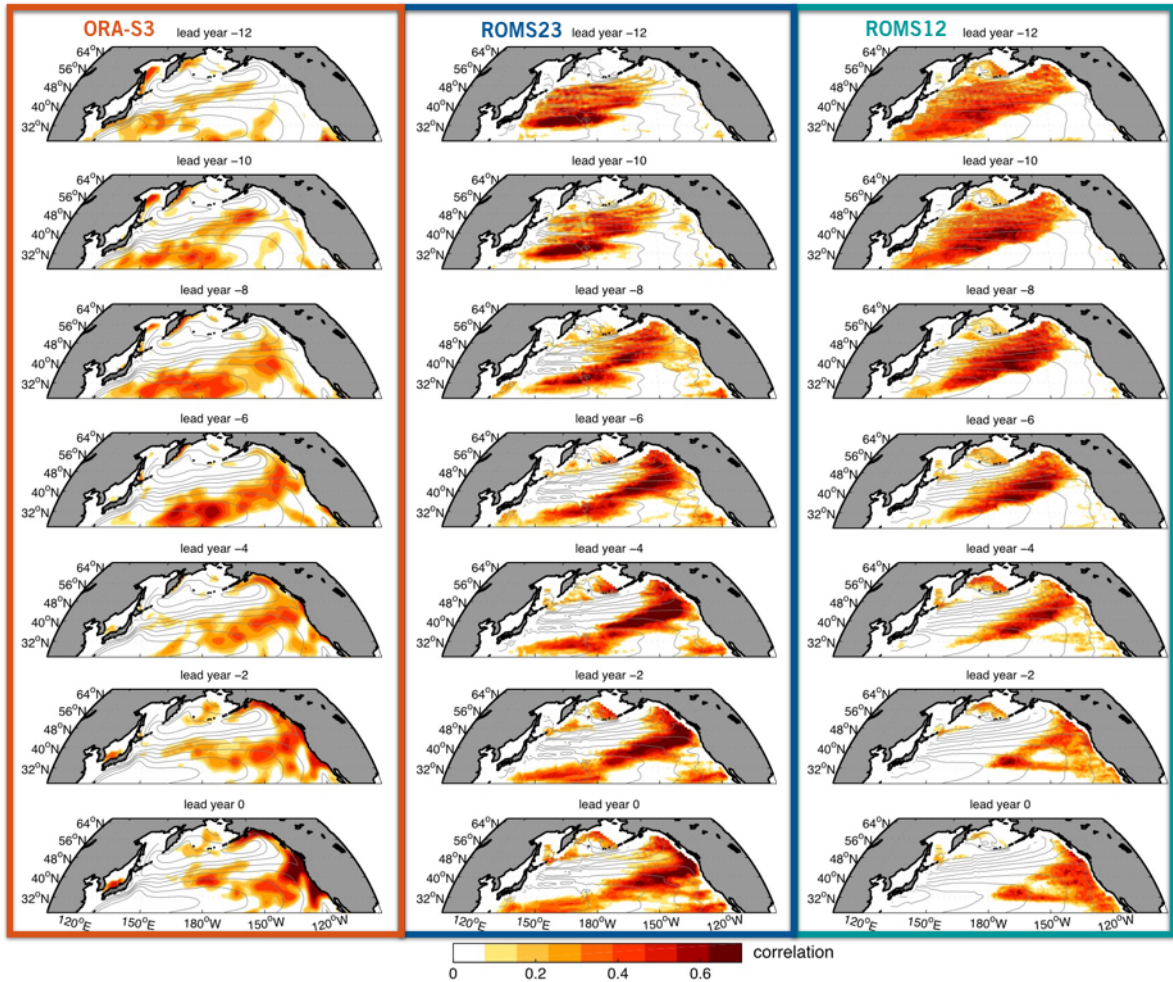
Figure 19. Subsurface propagation of salinity anomalies in ORA (a), ROMS23 (b), and ROMS12 (c). Lead correlation maps between the salinity anomalies on isopycnal 27 (isopycnal 26.9 for ROMS23) and the salinity PC1 from lead 12 years to 0 years, in increments of 2 years. Only positive correlations are plotted in the shading. Contours represent the mean Bernoulli's stream function along isopycnal 27 showing the path of the mean subsurface circulation. The salinity PC1 (red line Figures 22 b,c) is the time series of the leading mode of the salinity defined in the red box (Figure 22a, bottom panel on the left).

To further examine the eastward propagation of the subsurface salinity anomalies, we focus on the propagation along the North Pacific Current from the KOE to the CCS. The propagation of these anomalies from the KOE region in ROMS23 and ROMS12 and from NPC in ORA-S3 can be confirmed by Hovmöller diagrams of the previous average correlation maps (Figure 20). They show that strong (R>0.4) correlations between the

western boundary and CCS salinity anomalies appears around 12 years in the models and propagate eastward following the mean circulation path. In ROMS12 the correlation grows by year 10 and maintains that maximum until year 4. In contrast, the maximum correlation in ROMS23 is reached at lead 6 years, and maintained and expanded all the way until it reaches the CCS region. In ORA-S3, the maximum correlation is found in the region of the CCS and it is more clearly significant around year 8, as in *Pozo Buil and Di Lorenzo* [2017].
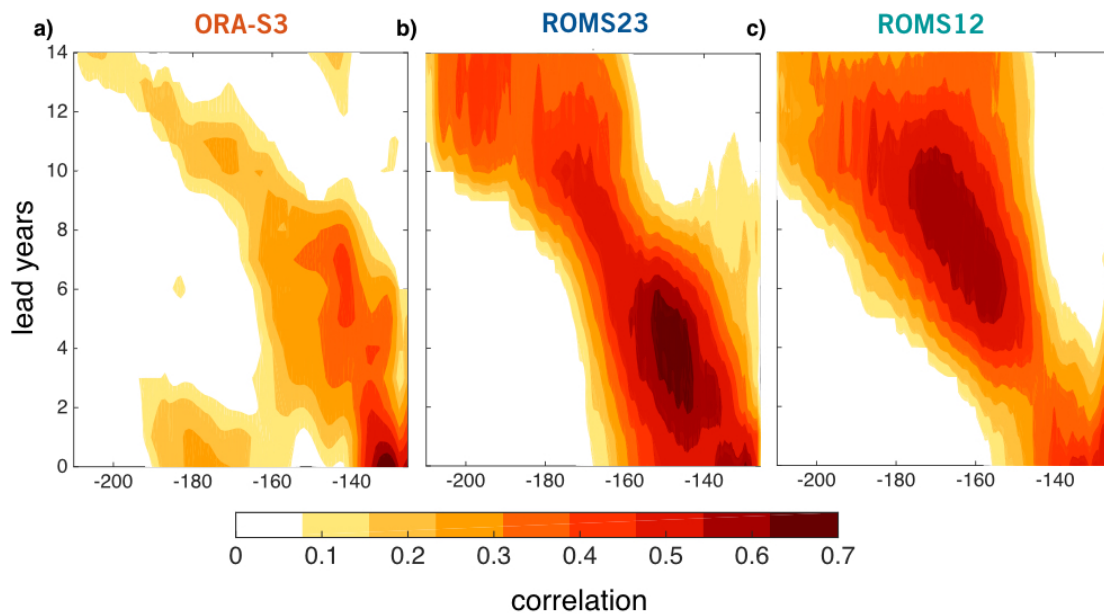
Figure 20. Hovmöller diagrams (time-longitude sections) of the correlation between the salinity anomalies on isopycnal 27 (isopycnal 26.9 for ROMS23) and the salinity PC1 averaged along the path of the North Pacific Current (150°E - 125°W, 38°N-46°N) from (a) ORA, (b) ROMS23, (c) and ROMS12.

Subsurface salinity anomalies along the NPC clearly propagate from the west to the east (Figure 21) on the isopycnal 27. On the western boundary, negatives anomalies were observed in 1960, 1985 and 1997, and positive anomalies around 1970, 1975, and 1990 in both models and in ORA-S3. In the models, some of anomalies move and reach around 140°W taking ~10 years. In the reanalysis, anomalies decay around 170°W, which make

some of them, hard to track. However, negative anomalies around 1995 in ORA-S3 and later around 1997 in ROMS23 and ROMS12, clearly propagate all the way to the eastern boundary. There is a good agreement in the sign of the anomalies between the models and ORA-S3, but the exception that the magnitude of the ROMS12 anomalies is half the magnitude found in the ROMS23 and ORA-S3 anomalies. This may be attributed to the higher intrinsic variability that we found when comparing ROMS12 vs. ROMS23 ensemble spread.
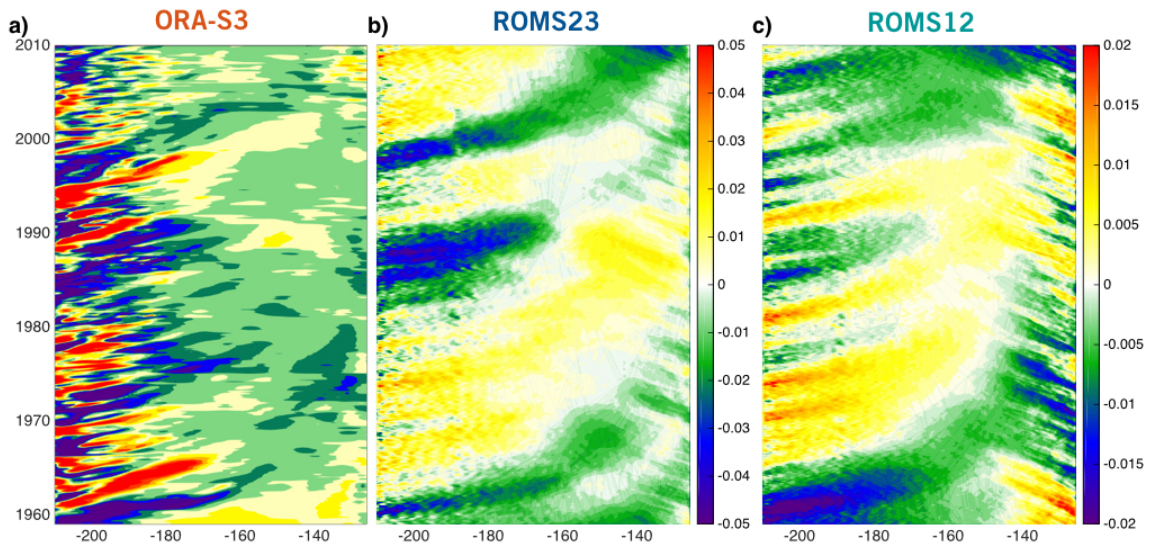
Figure 21. Hovmöller diagrams (time-longitude sections) of ensemble mean subsurface salinity anomalies along the mean propagation path found in Figure 19 (150°E - 125°W, 38°N- 46°N) from (a) ORA, (b) ROMS23, and (c) ROMS12.

The propagation speed on the isopycnal 27 are similar to the mean geostrophic velocities of about ~0.026 and 0.02 m s^{-1} (corresponding to ~6 years from 210°W to 160°W (~5600 km) in ROMS23 and ROMS12, respectively (Figure 22). A recent study, using ARGO, shows subsurface salinity anomalies propagating from the KOE to the NPC bifurcation region by mean geostrophic advection (~0.019 m s^{-1}, 7 years) [*Kouketsu et al.*, 2017]. From

63

140°W to the east, both models capture the signal of the salinity anomalies propagating from the coast, (as we can see in the direction of the currents in Figure 22).
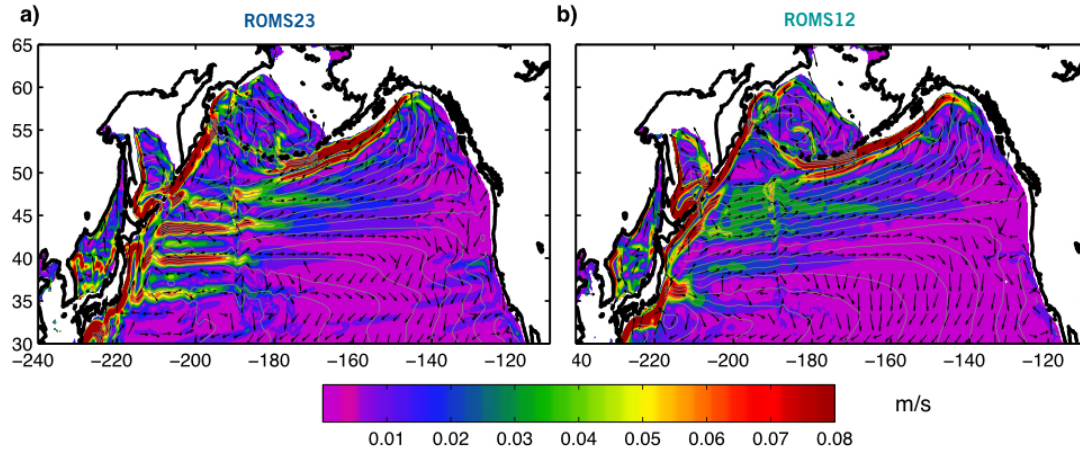
.Figure 22. Mean speed of the currents on the $\sigma_\theta = 27$ kg m^{-3} isopycnal surface from **(a) ROMS23 and (b) ROMS12 dataset (color shading). Black arrows represent the direction of the currents on isopycnal 27. Contours represent the mean Bernoulli's stream function along isopycnal 27 showing the path of the mean subsurface circulation.**

4.6   Quantifying the predictability arising from ROMS propagation dynamics

In this section, we quantify the decadal predictability of subsurface salinity in the CCS, associated with the propagation dynamics of the anomalies as they travel from the generation region. We focus on the decadal predictability by exploring the impact of different initial conditions and different resolutions of the two ensemble ROMS models. The two ensemble models are used to assess the statistical robustness and to sustain previous findings on the potential decadal predictability of the anomalies in the CCS associated with the advection along the gyre.

Following the same approach described in *Pozo Buil and Di Lorenzo* [2017], we compare the temporal variability between the subsurface salinity anomalies in KOE and NPC bifurcation regions with salinity anomalies in the CCS with the appropriate lags of 6 and 12 years later, respectively. We define indexes representative of each region: the KOE, NPC, and CCS index (Figure 23, panel b and c green, blue and red lines, respectively). These indexes are the average subsurface salinity anomalies in the regions delimitated by the green, blue, and red boxes in Figure 23a. An exact location of the boxes is described in caption of Figure 23. The CCS index (red line) corresponds with the PC1 of the salinity in the CCS region (same region as in *Pozo Buil and Di Lorenzo*, [2017]) and the NPC index (blue line) is the same as shown in Figure 17a, b. In ROMS23, time series of the indexes exhibit strong and significant correlation R=0.83 (CCS vs. NPC 6 years lead), R=0.67 (CCS vs. KOE 12 years lead), and R=0.66 (NPC and KOE 6 years lead) with a dominant multi-decadal signal. Similar multi-decadal variability is found when comparing the ROMS12 indexes. Although the magnitude and the significance of the correlation decrease in the finer resolution ensemble when comparing CCS vs. NPC 6 years lead (R=0.52,>88%), and CCS vs. KOE 12 years lead (R=0.53,>88%), we found a relative increase of the correlation (R=0.75,>95%) when comparing NPC vs. KOE 6 years in ROMS12 vs. ROMS23 indexes.
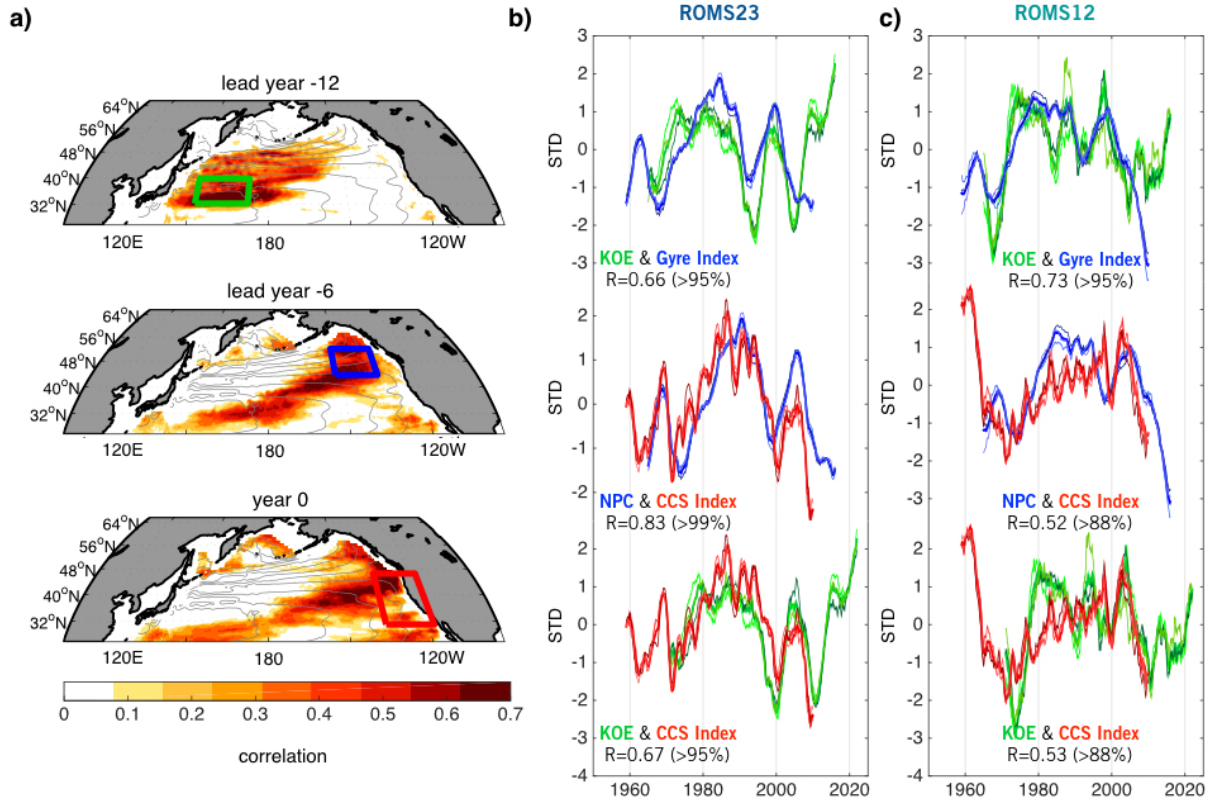
Figure 23. (a) Summary of the subsurface propagation of salinity anomalies on ROMS23 (same as in Figure 19b). The CCS index (red line in panel b and c) is obtained as the PC1 of the ensemble mean salinity anomalies within the red box (panel a, red box coordinates 136°W – 118°W and 31°N – 46.5°N). The NPC index (blue line in b and c) is defined as the spatially averaged salinity anomaly upstream the gyre in the region of the NPC bifurcation (blue box: 152.9°W – 135.4°W and 43.6°N – 52°N). The salinity KOE index (green line in b and c) is defined as the spatially averaged salinity anomaly in the region of the KOE (green box coordinates: 152°E – 188°W and 32.23°N – 39.7°N). The KOE index leads the salinity NPC and the CCS salinity index by 6 and 12 years, respectively. The NPC index leads the CCS index by 6 years. Bold lines represent the ensemble mean indexes and thin lines represent the individual indexes of each member of the ROMS23 (panel b) and ROMS12 (panel c) ensembles.

We further test the sensitivity skill of these decadal predictions by changing the position of the boxes where the indexes are defined, but fixing the position of the box of the CCS index (i.e., salinity PC1 in CCS region) in both models (Figure 24 panel a, red box). An exact position of the boxes is listed in Table 1. In Figure 24 (panels b and c), the shading

represents the spread of the solution obtained by moving the boxes in the two ROMS ensembles. We find that both models reproduce similar magnitude and significance of the correlation between the CCS and KOE anomalies 12 years in the KOE region (R=0.6,>93% in ROMS12 vs. R=0.66,>95% in ROMS23). Using anomalies from the NPC region the magnitude and significance of the correlation with the CCS anomalies slightly decrease (R=0.56,>87% in ROMS12 vs. R=0.86,>99% in ROMS23). Since the KOE index is defined in the region of the larger spread in both models, variability of the KOE is larger than the NPC when we select different boxes for the indexes in both models. Overall, the potential predictability of the subsurface salinity anomalies in the CCS is comparable in both ensemble models when we using anomalies that were generated 12 years before in the KOE region. However, when using anomalies from the NPC bifurcation region (6 years before), the potential decadal predictability in ROMS12 is limited by the oceanic intrinsic variability.

	Box 1	152.9°W – 135.4°W	43.6°N – 52°N
NPC	**Box 2**	156.5°W – 145.5°W	39.8°N – 46.1°N
	Box 3	150.9°W – 135.9°W	49.3°N – 52.2°N
	Box 1	152°E – 188°W	32.2°N – 39.7°N
KOE	**Box 2**	160.1°E – 182.6°W	43.4°N – 47.7°N
	Box 3	163.5°E – 178.8°W	33.1°N – 42.46°N

Table 1. Position of the boxes depicted in Figure 24
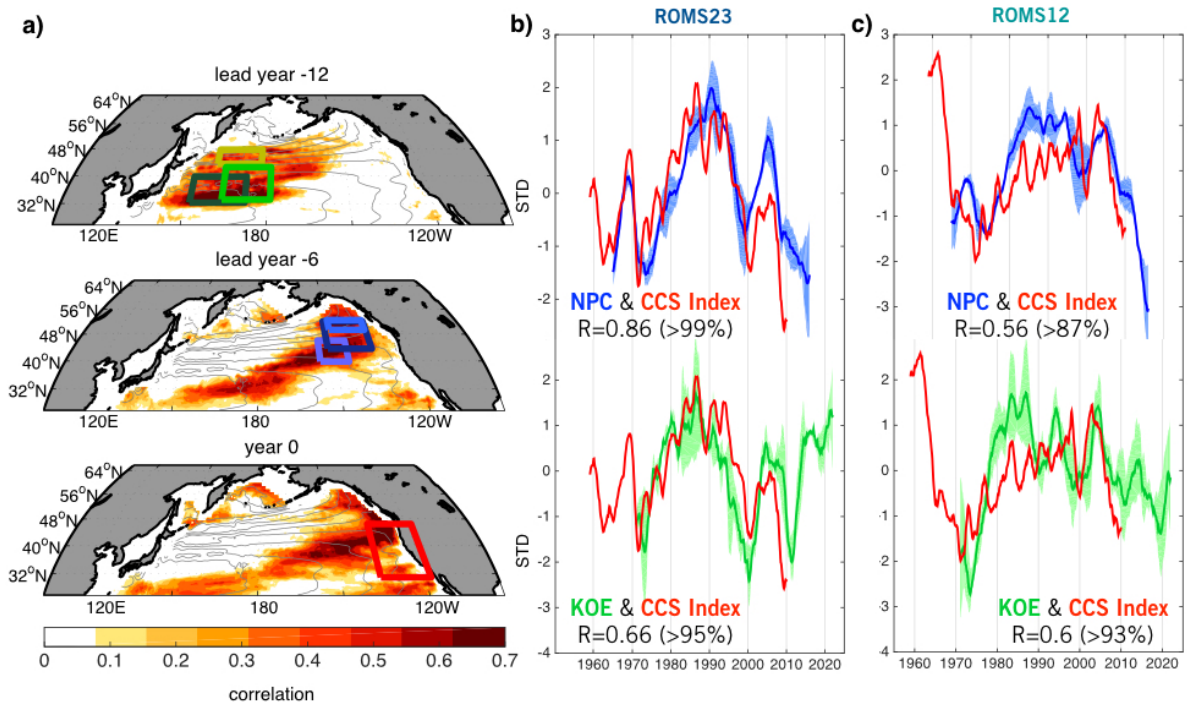
Figure 24. Same as Figure 23, except that KOE and NPC indices are computed over several spatial domains (see green and blue boxes in panel a) to test the sensitivity of the index to different definition of the areas used to average the salinity anomaly. In the time series plot, bold lines represent the average of the indices computed over the different boxes (i.e., blue = NPC boxes, green = KOE boxes) and shading shows the spread associated with individual indices from each boxes. The coordinates for the location of the boxes are listed in Table 1.

CHAPTER 5.   CONCLUSIONS AND DISCUSSION

The goal of this thesis was to to explore the dynamics of subsurface propagation of tracer anomalies in the Northeast Pacific using observations and models, and to quantify the decadal predictability of their impacts in the upwelling systems of the Gulf of Alaska and California Current System. We now briefly summarize the main contributions of this thesis and then discuss important questions that have emerged from it.

In Chapter 2, we showed that subsurface temperature anomalies propagated by mean advection along the North Pacific Current significantly contribute through mean upwelling to decadal changes of surface temperature in the Gulf of Alaska. We expanded the Ekman process model proposed by *Cummins and Lagerloef* [2002] to include the contributions of the mean upwelling acting on subsurface temperature anomalies at the base of the Ekman layer. The resulting linear model forced by Ekman pumping and subsurface temperature anomalies explained almost half of the multi-decadal low-frequency variance of the SST in the GOA. Using reanalysis data, we also showed that the influence of the subsurface anomalies in the surface temperature of the GOA is comparable to the contribution associated with variations in atmospheric winds.

We find that subsurface anomalies in the core of the North Pacific Current propagate temperature, salinity, and oxygen signals downstream into the coastal California Current upwelling system following the path of the mean gyre circulation with a timescale of ~10 years. We suggest these propagation dynamics lead to potential predictability of other quasi-passive tracers like oxygen.

In Chapter 3, we explored the role of the subsurface salinity anomalies on the isopycnal layer $\sigma_\theta = 26.5\ kg\ m^{-3}$ in modulating the low-frequency variability of subsurface oxygen content, an important water-mass property for ecosystems, in the CCS. We suggested that decadal changes observed in the oxygen content of the CCS upwelling source waters are primarily controlled by the transport of subsurface water mass anomalies associated with the mean gyre-scale circulation rather than by biological controls. We proposed subsurface salinity anomalies as a proxy for subsurface oxygen content in the CCS. We found that subsurface anomalies in the core of the North Pacific Current propagate downstream into the coastal upwelling system following the path of the mean gyre circulation with a timescale of ~10 years, which is consistent with the mean advection timescales estimated using the ORA-S3 reanalysis dataset. We also identified these propagation dynamics of the subsurface anomalies from upstream in the gyre as a potential mechanism for skillful reconstructions of the observed multi-decadal changes in oxygen and other passive tracers in the CCS. Based on the strong and significant relation between the anomalies in the CCS and the anomalies in the gyre ~10 years before, we also proposed a potential forecast of declining oxygen content of the source waters that feed the CCS upwelling by 2020.

Finally, in Chapter 4, we assessed the statistical robustness of the previous decadal forecasts of subsurface tracers in the CCS using an ensemble approach of retrospective ocean simulations for the period 1959-2009. The ensemble approach consisted of three members of the same model with non-eddy-resolving (~23 km, ROMS23) and eddy-resolving (~12 km, ROMS12) resolutions (a total of six members). To ensure that the subsurface ocean reaches a state of equilibrium, we ran a spin-up of more than one thousand

years with the non-eddy model. Both models adequately reproduce the vertical structure of the North Pacific and the subsurface low-frequency variability of the water-mass properties.

We identified a region of strong deterministic (i.e., predictable) variance in the core of the NPC and in the sub-polar gyre region. In the subtropical gyre, KOE, and CCS the variance is predominantly intrinsic. These regions of intrinsic and deterministic variance inferred from comparing the model ensemble members, are also consistent with comparison against the ocean reanalysis. We also used the two model ensembles to confirm the eastward propagation of the subsurface water-mass properties from NPC all the way from the western (KOE) to eastern (CCS) boundary of the North Pacific.

In addition, we quantified the predictability (i.e., deterministic vs. intrinsic variability) associated with the arrival of the subsurface anomalies in the CCS upwelling system. Overall, we found similar strong and significant correlation between CCS anomalies and their predictions using anomalies from the KOE region 12 years later in both models. However, when we considered anomalies from the NPC region (6 years later), we found higher predictability skill from the ROMS23 than from the ROMS12 model. This is caused by the fact that the region of the CCS exhibited more eddy variability and also more intrinsic variability in the ROMS12 than in the ROMS23 model. We also established that the skill of the decadal predictions is sensitive to the location of the box used for constructing the predictor index and to the model resolution (ROMS vs. ORA-S3).

There are further potential inquiries regarding this work that may be fruitful areas for future research. For instance, identifying the forcing mechanisms that modulate these low-

frequency changes in eddy-resolved circulation and water-mass anomalies in the subsurface North Pacific. Two hypotheses exist about the generation of the subsurface anomalies (1) subsurface anomalies are generated in the subduction regions in the KOE and propagated eastward by mean flow advection through the gyre [*Taguchi and Schneider*, 2014 and 2017], and (2) subsurface anomalies are also generated and amplified as they travel along isopycnals through anomalous advection [*Kilpatrick et al.,* 2011]. We showed that the subsurface anomalies propagate by mean advection, but they are also transformed from the generation region (KOE) to the eastern boundary, implying that the anomalous advection term (i.e., eddy-scale variability) plays some role in the transformation and propagation of the anomalies. Future research could attempt to use the ensemble models to test both hypotheses and to diagnose the forcing dynamics that drive the deterministic and predictable low-frequency variability of the subsurface anomalies.

Another interesting question to investigate relates to the subsurface anomalies in the CCS region. Although our results emphasize the role of the gyre circulation in driving multi-decadal subsurface tracer anomalies in the CCS, ROMS12 displays some correlation signals in the southern part of the CCS domain, near the Southern California Bight (Figure 19c) for lag 0 to lead 4 years, which may be associated with the CU dynamics. A closer look into the CCS with ROMS12 (e.g., by nesting a finer grid (~1km) in the eastern boundary) may able to separate and quantify the contribution of the two source waters to the decadal variability of water-mass properties.

Given the strong recent interest in the decadal timescale variability and the potential for its predictability, it becomes critical to identify dynamics that carry inherent decadal-scale predictability. This work provides evidence of the role of ocean subsurface circulation

dynamics as a source of decadal variability in the eastern North Pacific upwelling systems and may be a promising avenue for decadal predictability of key ecological and societally-relevant indicators.

APPENDIX A. SALINITY RESTORING APPROACH

The restoring salt flux in ROMS-UCLA is calculated according to:

$$Swflux_{restore} = V_{piston}(SSS_{obs} - SSS_{sim})$$ (4)

where SSS_{obs} and SSS_{sim} are the observed and simulated values respectively, and V_{piston} is a piston velocity. In our case, we restored the Swflux to ECMWF ORA-S3 time-dependent (i.e., 1959-2009) SSS. We initiated the spin-up simulation using a piston velocity of 3.5 cm d^{-1}, equivalent to ~50 m every 4 years (following *Yin et al.*, 2009). However, after 306 years the SSS variability in the model was not comparable with the forced data. To maintain a more realistic SSS mean state and to get a better representation of the model SSS variability, we increase the value of the V_{piston}. To find a new value of the V_{piston} we follow 2 approaches:

1) Using the variable dQdSST for restoring the SST (heat flux). In ROMS the flux of the T is calculated as:

$$stflux = stflux + dQdSSTt(t - St)$$ (5)

Where stflux is the kinematic surface temperature (heat) flux (°C m s^{-1}) or Kinematic surface freshwater flux (Evaporation-Precipitation) flux (PSU m s^{-1}), which varies spatially and seasonally. If we consider a mean value dQdSST of ~40.2 °C m s^{-1}, a mean sea water density of 1027.8. kg m^{-3}, and the specific heat of sea water at constant

pressure = 3985.0 J kg^{-1} C^{-1}, we obtain a new value V$_{new\_piston1}$ of 84.7 cm d^{-1} (~300 m yr^{-1})

2) Using the mean surface mixed layer depth of the last year of the simulation ~ 43 m (after 306 yr), we obtain a V$_{new\_piston2}$ of 143 cm d^{-1} (~516 m yr^{-1})

The final value of the V$_{new\_piston}$ is a compromise between the values the average obtained by these two approaches, ~100 cm d^{-1}.

REFERENCES

Balmaseda, M. A., A. Vidard, and D. L. T. Anderson (2008), The ECMWF Ocean Analysis System: ORA-S3, Mon Weather Rev, 136(8), 3018-3034, doi: 10.1175/2008mwr2433.1.

Barnett, T. P., D. W. Pierce, R. Saravanan, N. Schneider, D. Dommenget, and M. Latif (1999), Origins of the midlatitude Pacific decadal variability, Geophys Res Lett, 26(10), 1453-1456, doi: 10.1029/1999gl900278.

Barnier, B., L. Siefridt, and P. Marchesiello (1995), Thermal Forcing for a Global Ocean Circulation Model Using a 3-Year Climatology of Ecmwf Analyses, J Marine Syst, 6(4), 363-380, doi: Doi 10.1016/0924-7963(94)00034-9.

Bograd, S. J., C. G. Castro, E. Di Lorenzo, D. M. Palacios, H. Bailey, W. Gilly, and F. P. Chavez (2008), Oxygen declines and the shoaling of the hypoxic boundary in the California Current, Geophys Res Lett, 35(12), doi: Artn L12607Doi 10.1029/2008gl034185.

Bograd, S. J., M. P. Buil, E. Di Lorenzo, C. G. Castro, I. D. Schroeder, R. Goericke, C. R. Anderson, C. Benitez-Nelson, and F. A. Whitney (2015), Changes in source waters to the Southern California Bight, Deep-Sea Res Pt Ii, 112, 42-52, doi: DOI 10.1016/j.dsr2.2014.04.009.

Bopp, L., et al. (2013), Multiple stressors of ocean ecosystems in the 21st century: projections with CMIP5 models, Biogeosciences, 10(10), 6225-6245, doi: 10.5194/bg-10-6225-2013.

Cambon, G., K. Goubanova, P. Marchesiello, B. Dewitte, S. Illig, and V. Echevin (2013), Assessing the impact of downscaled winds on a regional ocean model simulation of the Humboldt system, Ocean Model, 65, 11-24, doi: 10.1016/j.ocemod.2013.01.007.

Carton, J. A., and B. S. Giese (2008), A Reanalysis of Ocean Climate Using Simple Ocean Data Assimilation (SODA), Mon Weather Rev, 136(8), 2999-3017, doi: 10.1175/2007mwr1978.1.

Checkley, D. M., and J. A. Barth (2009), Patterns and processes in the California Current System, Prog Oceanogr, 83(1-4), 49-64, doi: DOI 10.1016/j.pocean.2009.07.028.

Chhak, K. C., E. Di Lorenzo, N. Schneider, and P. F. Cummins (2009), Forcing of Low-Frequency Ocean Variability in the Northeast Pacific*, J Climate, 22(5), 1255-1276, doi: 10.1175/2008jcli2639.1.

Chikamoto, M. O., A. Timmermann, Y. Chikamoto, H. Tokinaga, and N. Harada (2015), Mechanisms and predictability of multiyear ecosystem variability in the North Pacific, Global Biogeochem Cy, 29(11), 2001-2019, doi: 10.1002/2015GB005096.

Chu, P. C., R. F. Li, and X. B. You (2002), Northwest Pacific subtropical countercurrent on isopycnal surface in summer, Geophys Res Lett, 29(17), doi: Artn 1842Doi 10.1029/2002gl014831.

Combes, V., and E. Di Lorenzo (2007), Intrinsic and forced interannual variability of the Gulf of Alaska mesoscale circulation, Prog Oceanogr, 75(2), 266-286, doi: DOI 10.1016/j.pocean.2007.08.011.

Connolly, T. P., B. M. Hickey, S. L. Geier, and W. P. Cochlan (2010), Processes influencing seasonal hypoxia in the northern California Current System, J Geophys Res-Oceans, 115, doi: Artn C0302110.1029/2009jc005283.

Crawford, W., J. Galbraith, and N. Bolingbroke (2007), Line P ocean temperature and salinity, 1956-2005, Prog Oceanogr, 75(2), 161-178, doi: DOI 10.1016/j.pocean.2007.08.017.

Crawford, W. R., and M. A. Pena (2016), Decadal Trends in Oxygen Concentration in Subsurface Waters of the Northeast Pacific Ocean, Atmos Ocean, 54(2), 171-192, doi: 10.1080/07055900.2016.1158145.

Cummins, P. F., and G. S. E. Lagerloef (2002), Low-frequency pycnocline depth variability at Ocean Weather Station P in the northeast Pacific, J Phys Oceanogr, 32(11), 3207-3215, doi: Doi 10.1175/1520-0485(2002)032<3207:Lfpdva>2.0.Co;2.

Curchitser, E. N., D. B. Haidvogel, A. J. Hermann, E. L. Dobbins, T. M. Powell, and A. Kaplan (2005), Multi-scale modeling of the North Pacific Ocean: Assessment and analysis of simulated basin-scale variability (1996-2003), J Geophys Res-Oceans, 110(C11), doi: Artn C11021Doi 10.1029/2005jc002902.

Deutsch, C., H. Brix, T. Ito, H. Frenzel, and L. Thompson (2011), Climate-Forced Variability of Ocean Hypoxia, Science, 333(6040), 336-339, doi: DOI 10.1126/science.1202422.

Di Lorenzo, E., and M. D. Ohman (2013), A double-integration hypothesis to explain ocean ecosystem response to climate forcing, P Natl Acad Sci USA, 110(7), 2496-2499, doi: DOI 10.1073/pnas.1218022110.

Di Lorenzo, E., A. J. Miller, N. Schneider, and J. C. McWilliams (2005), The warming of the California current system: Dynamics and ecosystem implications, J Phys Oceanogr, 35(3), 336-362, doi: Doi 10.1175/Jpo-2690.1.

Di Lorenzo, E., et al. (2008), North Pacific Gyre Oscillation links ocean climate and ecosystem change, Geophys Res Lett, 35(8), doi: Artn L08607 Doi 10.1029/2007gl032838.

Diaz, R. J., and R. Rosenberg (2008), Spreading dead zones and consequences for marine ecosystems, Science, 321(5891), 926-929, doi: DOI 10.1126/science.1156401.

Freeland, H. (2007), A short history of ocean station papa and Line P, Prog Oceanogr, 75(2), 120-125, doi: DOI 10.1016/j.pocean.2007.08.005.

Gay, P. S., and T. K. Chereskin (2009), Mean structure and seasonal variability of the poleward undercurrent off southern California, J Geophys Res-Oceans, 114, doi: Artn C0200710.1029/2008jc004886.

Griffies, S. M., et al. (2009), Coordinated Ocean-ice Reference Experiments (COREs), Ocean Model, 26(1-2), 1-46, doi: 10.1016/j.ocemod.2008.08.007.

Haidvogel, D. B., H. G. Arango, K. Hedstrom, A. Beckmann, P. Malanotte-Rizzoli, and A. F. Shchepetkin (2000), Model evaluation experiments in the North Atlantic Basin: simulations in nonlinear terrain-following coordinates, Dynam Atmos Oceans, 32(3-4), 239-281, doi: Doi 10.1016/S0377-0265(00)00049-X.

Hasselmann, K. (1976), Stochastic Climate Models .1. Theory, Tellus, 28(6), 473-485.

Hauri, C., N. Gruber, Z. Lachkar, and G. K. Plattner (2009), Accelerated acidification in eastern boundary current systems, Geochim Cosmochim Ac, 73(13), A503-A503.

Hauri, C., N. Gruber, M. Vogt, S. C. Doney, R. A. Feely, Z. Lachkar, A. Leinweber, A. M. P. McDonnell, M. Munnich, and G. K. Plattner (2013), Spatiotemporal variability and long-term trends of ocean acidification in the California Current System, Biogeosciences, 10(1), 193-216, doi: 10.5194/bg-10-193-2013.

Hermann, A. J., S. Hinckley, E. L. Dobbins, D. B. Haidvogel, N. A. Bond, C. Mordy, N. Kachel, and P. J. Stabeno (2009), Quantifying cross-shelf and vertical nutrient flux in the Coastal Gulf of Alaska with a spatially nested, coupled biophysical model, Deep-Sea Res Pt Ii, 56(24), 2474-2486, doi: 10.1016/j.dsr2.2009.02.008.

Hickey, B. M. (1979), The California current system—hypotheses and facts, Prog Oceanogr, 8(4), 191-279, doi: http://dx.doi.org/10.1016/0079-6611(79)90002-8.

Hinckley, S., K. O. Coyle, G. Gibson, A. J. Hermann, and E. L. Dobbins (2009), A biophysical NPZ model with iron for the Gulf of Alaska: Reproducing the differences between an oceanic HNLC ecosystem and a classical northern temperate shelf ecosystem, Deep-Sea Res Pt Ii, 56(24), 2520-2536, doi: 10.1016/j.dsr2.2009.03.003.

Ito, T., and C. Deutsch (2010), A conceptual model for the temporal spectrum of oceanic oxygen variability, Geophys Res Lett, 37, doi: Artn L03601Doi 10.1029/2009gl041595.

Jacox, M. G., A. M. Moore, C. A. Edwards, and J. Fiechter (2014), Spatially resolved upwelling in the California Current System and its connections to climate variability, Geophys Res Lett, 41(9), 3189-3196, doi: Doi 10.1002/2014gl059589.

Kalnay, E., et al. (1996), The NCEP/NCAR 40-year reanalysis project, B Am Meteorol Soc, 77(3), 437-471, doi: Doi 10.1175/1520-0477(1996)077<0437:Tnyrp>2.0.Co;2.

Kay, J. E., et al. (2015), THE COMMUNITY EARTH SYSTEM MODEL (CESM) LARGE ENSEMBLE PROJECT A Community Resource for Studying Climate Change in the Presence of Internal Climate Variability, B Am Meteorol Soc, 96(8), 1333-1349, doi: 10.1175/Bams-D-13-00255.1.

Kilpatrick, T., N. Schneider, and E. Di Lorenzo (2011), Generation of Low-Frequency Spiciness Variability in the Thermocline, J Phys Oceanogr, 41(2), 365-377, doi: Doi 10.1175/2010jpo4443.1.

Koslow, J. A., R. Goericke, A. Lara-Lopez, and W. Watson (2011), Impact of declining intermediate-water oxygen on deepwater fishes in the California Current, Mar Ecol Prog Ser, 436, 207-218, doi: Doi 10.3354/Meps09270.

Kouketsu, S., S. Osafune, Y. Kumamoto, and H. Uchida (2017), Eastward salinity anomaly propagation in the intermediate layer of the North Pacific, J Geophys Res-Oceans, 122(2), 1590-1607, doi: 10.1002/2016jc012118.

Large, W. G., J. C. Mcwilliams, and S. C. Doney (1994), Oceanic Vertical Mixing - a Review and a Model with a Nonlocal Boundary-Layer Parameterization, Reviews of Geophysics, 32(4), 363-403, doi: Doi 10.1029/94rg01872.

Latif, M., and N. S. Keenlyside (2011), A perspective on decadal climate variability and predictability, Deep-Sea Res Pt Ii, 58(17-18), 1880-1894, doi: DOI 10.1016/j.dsr2.2010.10.066.

Liu, Z. (2012), Dynamics of Interdecadal Climate Variability: A Historical Perspective*, J Climate, 25(6), 1963-1995, doi: 10.1175/2011jcli3980.1.

Liu, Z., L. Wu, R. Gallimore, and R. Jacob (2002), Search for the origins of Pacific decadal climate variability, Geophys Res Lett, 29(10), 42-41-42-44, doi: 10.1029/2001gl013735.

Liu, Z. Y. and E. Di Lorenzo, 2017: Mechanisms and Predictability of Pacific Decadal Variability. Current Climate Change Reports, in press

Long, M. C., C. Deutsch, and T. Ito (2016), Finding forced trends in oceanic oxygen, Global Biogeochem Cy, 30(2), 381-397, doi: 10.1002/2015GB005310.

Lynn, R. J., and J. J. Simpson (1987), The California Current System - the Seasonal Variability of Its Physical Characteristics, J Geophys Res-Oceans, 92(C12), 12947-&, doi: DOI 10.1029/JC092iC12p12947.

Mantua, N. J., S. R. Hare, Y. Zhang, J. M. Wallace, and R. C. Francis (1997), A Pacific interdecadal climate oscillation with impacts on salmon production, B Am Meteorol Soc, 78(6), 1069-1079, doi: Doi 10.1175/1520-0477(1997)078<1069:Apicow>2.0.Co;2.

McClatchie, S., R. Goericke, R. Cosgrove, G. Auad, and R. Vetter (2010), Oxygen in the Southern California Bight: Multidecadal trends and implications for demersal fisheries, Geophys Res Lett, 37, doi: Artn L19602Doi 10.1029/2010gl044497.

Meehl, G. A., A. X. Hu, and B. D. Santer (2009), The Mid-1970s Climate Shift in the Pacific and the Relative Roles of Forced versus Inherent Decadal Variability, J Climate, 22(3), 780-792, doi: Doi 10.1175/2008jcli2552.1.

Meehl, G. A., et al. (2014), Decadal Climate Prediction an Update from the Trenches, B Am Meteorol Soc, 95(2), 243-267, doi: Doi 10.1175/Bams-D-12-00241.1.

Mehta, V., G. Meehl, L. Goddard, J. Knight, A. Kumar, M. Latif, T. Lee, A. Rosati, and D. Stammer (2011), Decadal Climate Predictability and Prediction Where Are We?, B Am Meteorol Soc, 92(5), 637-640, doi: Doi 10.1175/2010bams3025.1.

Meinvielle, M., and G. C. Johnson (2013), Decadal water-property trends in the California Undercurrent, with implications for ocean acidification, J Geophys Res-Oceans, 118(12), 6687-6703, doi: 10.1002/2013JC009299.

Moore, A. M., H. G. Arango, G. Broquet, B. S. Powell, A. T. Weaver, and J. Zavala-Garay (2011a), The Regional Ocean Modeling System (ROMS) 4-dimensional variational data assimilation systems Part I - System overview and formulation, Prog Oceanogr, 91(1), 34-49, doi: DOI 10.1016/j.pocean.2011.05.004.

Moore, A. M., H. G. Arango, G. Broquet, C. Edwards, M. Veneziani, B. Powell, D. Foley, J. D. Doyle, D. Costa, and P. Robinson (2011b), The Regional Ocean Modeling System (ROMS) 4-dimensional variational data assimilation systems Part II - Performance and application to the California Current System, Prog Oceanogr, 91(1), 50-73, doi: DOI 10.1016/j.pocean.2011.05.003.

Nam, S., Y. Takeshita, C. A. Frieder, T. Martz, and J. Ballard (2015), Seasonal advection of Pacific Equatorial Water alters oxygen and pH in the Southern California Bight, J Geophys Res-Oceans, 120(8), 5387-5399, doi: 10.1002/2015jc010859.

Nonaka, M., and S.-P. Xie (2000), Propagation of North Pacific interdecadal subsurface temperature anomalies in an ocean GCM, Geophys Res Lett, 27(22), 3747-3750, doi: 10.1029/2000gl011488.

Osafune, S., and I. Yasuda (2013), Remote impacts of the 18.6 year period modulation of localized tidal mixing in the North Pacific, J Geophys Res-Oceans, 118(6), 3128-3137, doi: 10.1002/jgrc.20230.

Penven, P., L. Debreu, P. Marchesiello, and J. C. McWilliams (2006), Evaluation and application of the ROMS 1-way embedding procedure to the central california upwelling system, Ocean Model, 12(1-2), 157-187, doi: DOI 10.1016/j.ocemod.2005.05.002.

Penven, P., V. Echevin, J. Pasapera, F. Colas, and J. Tam (2005), Average circulation, seasonal cycle, and mesoscale dynamics of the Peru Current System: A modeling approach, J Geophys Res-Oceans, 110(C10), doi: Artn C10021Doi 10.1029/2005jc002945.

Peterson, J. O., C. A. Morgan, W. T. Peterson, and E. Di Lorenzo (2013), Seasonal and interannual variation in the extent of hypoxia in the northern California Current from 1998-2012, Limnol Oceanogr, 58(6), 2279-2292, doi: DOI 10.4319/lo.2013.58.6.2279.

Pierce, S. D., J. A. Barth, R. K. Shearman, and A. Y. Erofeev (2012), Declining Oxygen in the Northeast Pacific, J Phys Oceanogr, 42(3), 495-501, doi: Doi 10.1175/Jpo-D-11-0170.1.

Pozo Buil, M., and E. Di Lorenzo (2015), Decadal changes in Gulf of Alaska upwelling source waters, Geophys Res Lett, 42(5), 1488-1495, doi: 10.1002/2015gl063191.

Pozo Buil, M., and E. Di Lorenzo (2017), Decadal dynamics and predictability of oxygen and subsurface tracers in the California Current System, Geophys Res Lett, 44(9), 4204-4213, doi: 10.1002/2017gl072931.

Rabalais, N. N., R. J. Diaz, L. A. Levin, R. E. Turner, D. Gilbert, and J. Zhang (2010), Dynamics and distribution of natural and human-caused hypoxia, Biogeosciences, 7(2), 585-619.

Rudnick, D. L., and R. E. Davis (2003), Red noise and regime shifts, Deep-Sea Res Pt I, 50(6), 691-699, doi: Doi 10.1016/S0967-0637(03)00053-0.

Rykaczewski, R. R., and J. P. Dunne (2010), Enhanced nutrient supply to the California Current Ecosystem with global warming and increased stratification in an earth system model, Geophys Res Lett, 37, doi: Artn L21606Doi 10.1029/2010gl045019.

Sasaki, Y. N., N. Schneider, N. Maximenko, and K. Lebedev (2010), Observational evidence for propagation of decadal spiciness anomalies in the North Pacific, Geophys Res Lett, 37(7), n/a-n/a, doi: 10.1029/2010gl042716.

Schneider, N. (2000), A decadal spiciness mode in the tropics, Geophys Res Lett, 27(2), 257-260, doi: 10.1029/1999gl002348.

Schneider, N., and B. D. Cornuelle (2005), The forcing of the Pacific decadal oscillation, Journal of Climate, 18(21), 4355-4373, doi: 10.1175/jcli3527.1.

Schneider, N., A. J. Miller, and D. W. Pierce (2002), Anatomy of North Pacific decadal variability, J Climate, 15(6), 586-605, doi: Doi 10.1175/1520-0442(2002)015<0586:Aonpdv>2.0.Co;2.

Shchepetkin, A. F., and J. C. McWilliams (1998), Quasi-monotone advection schemes based on explicit locally adaptive dissipation, Mon Weather Rev, 126(6), 1541-1580, doi: Doi 10.1175/1520-0493(1998)126<1541:Qmasbo>2.0.Co;2.

Shchepetkin, A. F., and J. C. McWilliams (2003), A method for computing horizontal pressure-gradient force in an oceanic model with a nonaligned vertical coordinate, J Geophys Res-Oceans, 108(C3), doi: Artn 3090Doi 10.1029/2001jc001047.

Shchepetkin, A. F., and J. C. McWilliams (2005), The regional oceanic modeling system (ROMS): a split-explicit, free-surface, topography-following-coordinate oceanic model,Ocean Model, 9(4), 347-404, doi: DOI 10.1016/j.ocemod.2004.08.002.

Shchepetkin, A. F., and J. C. McWilliams (2009), Computational Kernel Algorithms for Fine-Scale, Multiprocess, Longtime Oceanic Simulations, Handb Num Anal, 14, 121-183, doi: Doi 10.1016/S1570-8659(08)01202-0.

Smith, T. M., and R. W. Reynolds (2003), Extended reconstruction of global sea surface temperatures based on COADS data (1854-1997), J Climate, 16(10), 1495-1510, doi: Doi 10.1175/1520-0442-16.10.1495.

Smith, T. M., and R. W. Reynolds (2004), Improved extended reconstruction of SST (1854-1997), J Climate, 17(12), 2466-2477, doi: Doi 10.1175/1520-0442(2004)017<2466:Ieros>2.0.Co;2.

Smith, T. M., R. W. Reynolds, T. C. Peterson, and J. Lawrimore (2008), Improvements to NOAA's historical merged land-ocean surface temperature analysis (1880-2006), J Climate, 21(10), 2283-2296, doi: Doi 10.1175/2007jcli2100.1.

Song, Y. H., and D. Haidvogel (1994), A Semiimplicit Ocean Circulation Model Using a Generalized Topography-Following Coordinate System, J Comput Phys, 115(1), 228-244, doi: DOI 10.1006/jcph.1994.1189.

Stramma, L., S. Schmidtko, L. A. Levin, and G. C. Johnson (2010), Ocean oxygen minima expansions and their biological impacts, Deep-Sea Res Pt I, 57(4), 587-595, doi: DOI 10.1016/j.dsr.2010.01.005.

Taguchi, B., and N. Schneider (2014), Origin of Decadal-Scale, Eastward-Propagating Heat Content Anomalies in the North Pacific, J Climate, 27(20), 7568-7586, doi: Doi 10.1175/Jcli-D-13-00102.1.

Taguchi, B., N. Schneider, M. Nonaka, and H. Sasaki (2017), Decadal Variability of Upper-Ocean Heat Content Associated with Meridional Shifts of Western Boundary Current Extensions in the North Pacific, J Climate, 30(16), 6247-6264, doi: 10.1175/Jcli-D-16-0779.1.

Talley, L. D. (1993), Distribution and Formation of North Pacific Intermediate Water, J Phys Oceanogr, 23(3), 517-537, doi: Doi 10.1175/1520-0485(1993)023<0517:Dafonp>2.0.Co;2.

Thomson, R. E., and M. V. Krassovski (2010), Poleward reach of the California Undercurrent extension, J Geophys Res-Oceans, 115, doi: Artn C0902710.1029/2010jc006280.

Unesco (1983), Algorithms for computation of fundamental properties of seawater, 1983. Unesco Tech. Pap. in Mar. Sci., No. 44, 53 pp

Veronis, G. (1972), Properties of Seawater Defined by Temperature, Salinity, and Pressure, J Mar Res, 30(2), 227-&.

Wallace, J. M., and D. S. Gutzler (1981), Teleconnections in the Geopotential Height Field during the Northern Hemisphere Winter, Mon Weather Rev, 109(4), 784-812, doi: Doi 10.1175/1520-0493(1981)109<0784:Titghf>2.0.Co;2.

Whitney, F. A., H. J. Freeland, and M. Robert (2007), Persistently declining oxygen levels in the interior waters of the eastern subarctic Pacific, Prog Oceanogr, 75(2), 179-199, doi: DOI 10.1016/j.pocean.2007.08.007.

Wyrtki, K. (1962), The Oxygen Minima in Relation to Ocean Circulation, Deep-Sea Research, 9(1), 11-23, doi: Doi 10.1016/0011-7471(62)90243-7.

Yin, J., E. Chassignet, W. G Large, N. J Norton, A. J Wallcraft, and S. Yeager (2009), Salinity Boundary Conditions and the Atlantic Meridional Overturning Circulation in Depth and Quasi-Isopycnic Coordinate Global Ocean Models.